

Supporting Information

Compatibility Score for Rational Electrophile Selection in Pd/NBE Cooperative Catalysis

Xiaotian Qi,[†] Jianchun Wang,[§] Zhe Dong,[§] Guangbin Dong,^{*,§} and Peng Liu^{*,†,‡}

[†]Department of Chemistry, University of Pittsburgh, Pittsburgh, PA 15260, USA

[§]Department of Chemistry, University of Chicago, Chicago, Illinois 60637, USA

[‡]Department of Chemical and Petroleum Engineering, University of Pittsburgh, Pittsburgh, PA
15261, USA

*Correspondence to: gbdong@uchicago.edu, pengliu@pitt.edu

Table of Contents

1. Relative free energies of possible ANP species	S3
2. S _E Ar mechanism for the C–N bond formation.....	S4
3. Alternative pathway of the concerted metallation-deprotonation (CMD) with Cs ₂ CO ₃	S5
4. Disfavored reaction pathways of neutral ANP oxidation with morpholino benzoate (EY-1)	S6
5. Disfavored reaction pathways of the oxidation of iodide-bound anionic ANP with EY-1...	S9
6. Reaction pathways of the oxidation of the BzO ⁻ -bound anionic ANP with EY-1	S12
7. Reaction pathways of β-carbon elimination and hydride transfer from Pd(II) complexes .	S16
8. Activation free energies of C–C reductive elimination from various ANP complexes	S18
9. Concerted and S _N 2-type oxidative addition transition states of Pd(0) and ANP-4 oxidation with various Ar–X and E–Y	S19
10. Concerted oxidative addition and S _N 2-type transition states of BzO ⁻ -bound anionic ANP	S24
11. Optimized structures of oxidative addition transition states and distortion-interaction analysis	S25
12. Comparison between open-shell and closed-shell singlet Pd oxidation transition states .	S30
13. Calculated bond dissociation energies (BDE) of Ar–X and E–Y	S31
14. Calculated ECS of amination and acylation with other electrophiles, aryl halides, and phosphine ligands	S32

15. Predicted compatibility scores (ECS) of electrophiles (EY-1~9) with different aryl halides (ArX-1~5).....	S37
16. Anion effects on the pathway selectivity of C–N reductive elimination	S38
17. Experimental procedure	S39
18. X-ray crystallography data	S43
19. References	S44

1. Relative free energies of possible ANP species

Under the catalytic conditions, several three- and four-coordinated ANP species supported by phosphine or anionic ligands may exist in equilibrium. Besides the six ANP complexes (ANP-1~6) shown in Fig. 2a, other possible neutral and anionic ANP complexes are summarized in Fig. S1. These ANP complexes have relatively high Gibbs free energies. Moreover, our computational studies suggested that subsequent ANP oxidation and C–N bond formation from these ANP complexes also have higher energy barriers. The detailed free energy profiles are discussed in the following sections.

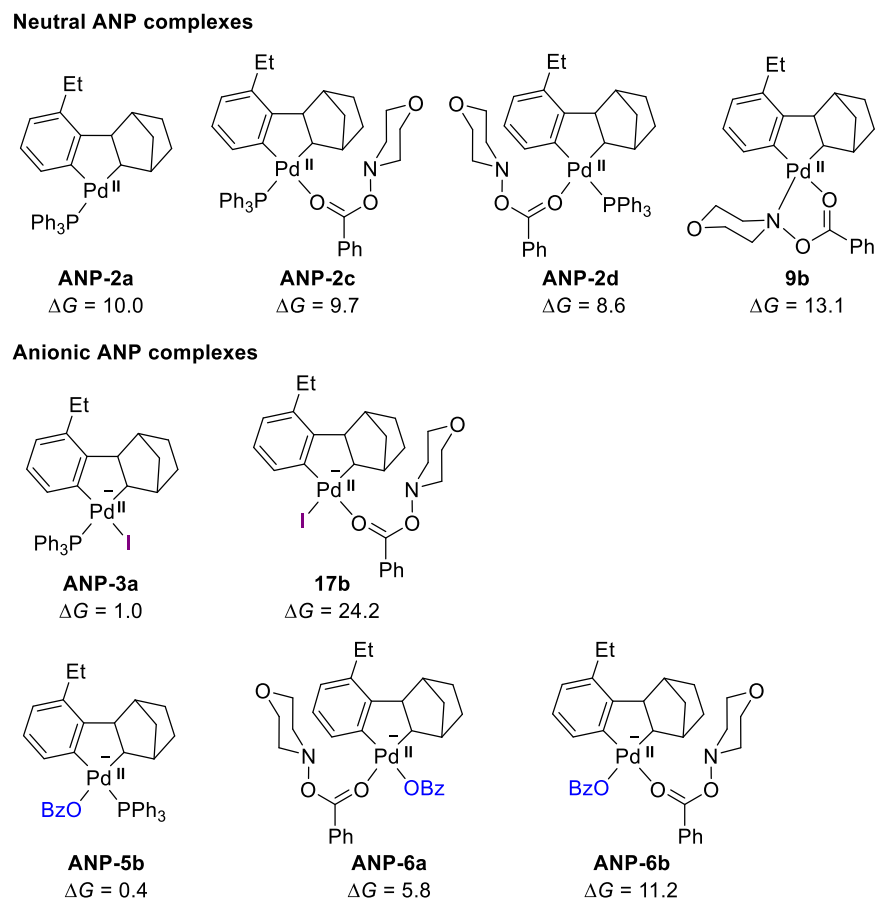


Fig. S1 The relative free energies of other possible ANP species considered in this study. All energies are in kcal/mol with respect to ANP-1.

2. S_EAr mechanism for the C–N bond formation

The S_EAr mechanism for the C–N bond formation was also considered. As shown in Fig. S2, the S_EAr transition state **TS-16** was located for the reaction between **ANP-6** and **EY-1**. However, this transition state has an activation free energy of 49.6 kcal/mol, which suggests this mechanism is highly disfavored for the C–N bond formation. We also tried to locate analogous transition states with other ANP complexes but failed to obtain other S_EAr transition states. We expect the neutral ANP complexes to be even less reactive in S_EAr than **ANP-6**. In addition, the σ -bond metathesis mechanism for C–N bond formation was also studied by calculations. However, attempts to locate the σ -bond metathesis transition states have failed. We surmise that the rigidity of the fused rings in ANP complexes suppresses the σ -bond metathesis mechanism because the benzene ring is locked in a co-planar geometry in the square-planar Pd(II) complex.

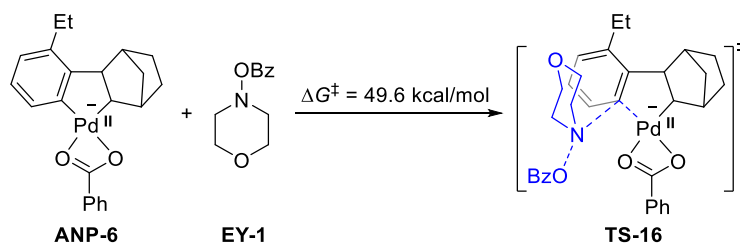


Fig. S2 S_EAr transition state **TS-16** for the C–N bond formation.

3. Alternative pathway of the concerted metallation-deprotonation (CMD) with Cs₂CO₃

An alternative pathway of the concerted metallation-deprotonation (CMD) with Cs₂CO₃ is shown in Fig. S3. Cs₂CO₃ can coordinate with the metal center through ligand exchange, which generates intermediate **4b**. This step is exergonic by 10.4 kcal/mol. Subsequent C–H activation could take place through the CMD transition state **TS-3b** with an activation free energy of 24.1 kcal/mol. **ANP-2** is then formed with concomitant release of CsHCO₃. Compared with the analogous CMD transition state **TS-3** in Fig. 1, this CMD pathway via **TS-3b** has a higher energy barrier ($\Delta\Delta G^\ddagger = 2.8$ kcal/mol).

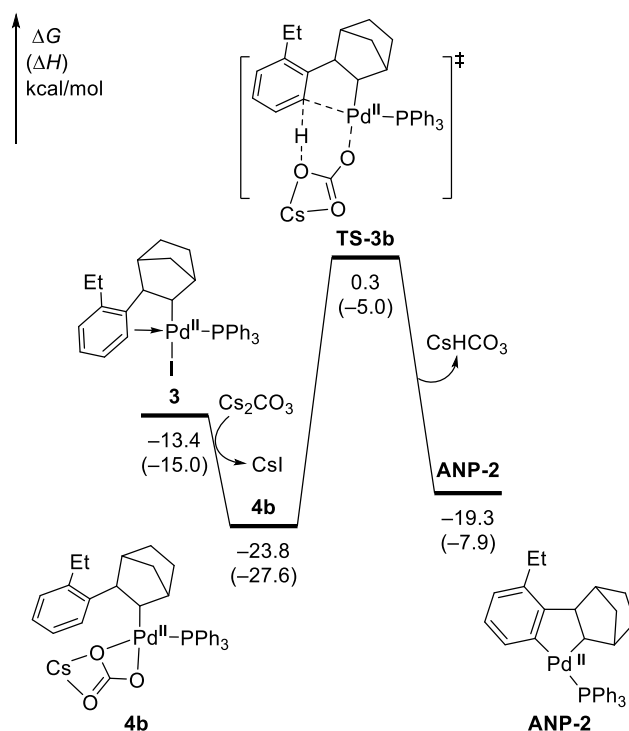


Fig. S3 Alternative pathway of the concerted metallation-deprotonation (CMD) with Cs₂CO₃.

4. Disfavored reaction pathways of neutral ANP oxidation with morpholino benzoate (EY-1)

The oxidative addition of morpholino benzoate (**EY-1**) to neutral ANP complexes can occur through concerted oxidative addition mechanism or S_N2 -type mechanism. Because several three- and four-coordinated ANP species supported by phosphine or anionic ligands may exist in equilibrium under the catalytic conditions, the corresponding ANP oxidation transition states could have different mechanisms and diverse coordination environments. Besides the free energy profiles shown in Fig. 3, other disfavored reaction pathways of neutral ANP oxidation with **EY-1** are shown in Fig. S4 and S5. The following C–N bond formation through C–N reductive elimination was also studied.

As shown in Fig. S4, a five-membered cyclic transition state **TS-7b** was located for the concerted oxidative addition of **EY-1** to **ANP-1**. This transition state is a conformer of **TS-7** (Fig. 3a) and they have comparable energy barriers. The oxidative addition pathways lead to Pd(IV) intermediate **10b**, which could isomerize to **10** and then undergo C(sp^3)–N reductive elimination via **TS-8b**. Compared with the C(sp^2)–N reductive elimination transition state **TS-8** (Fig. 3a), the C(sp^3)–N reductive elimination has a higher energy barrier ($\Delta\Delta G^\ddagger = 5.4$ kcal/mol) due to steric hindrance around the sp^3 -hybridized carbon. In addition, another Pd(IV) complex **10c**, which can be formed via isomerization of **10** or **10b**, was located. This complex has a 7.3 kcal/mol higher free energy than **10b**. Subsequent C(sp^2)–N and C(sp^3)–N reductive elimination from **10c** occur through the same transition states (**TS-8** and **TS-8b**, respectively).

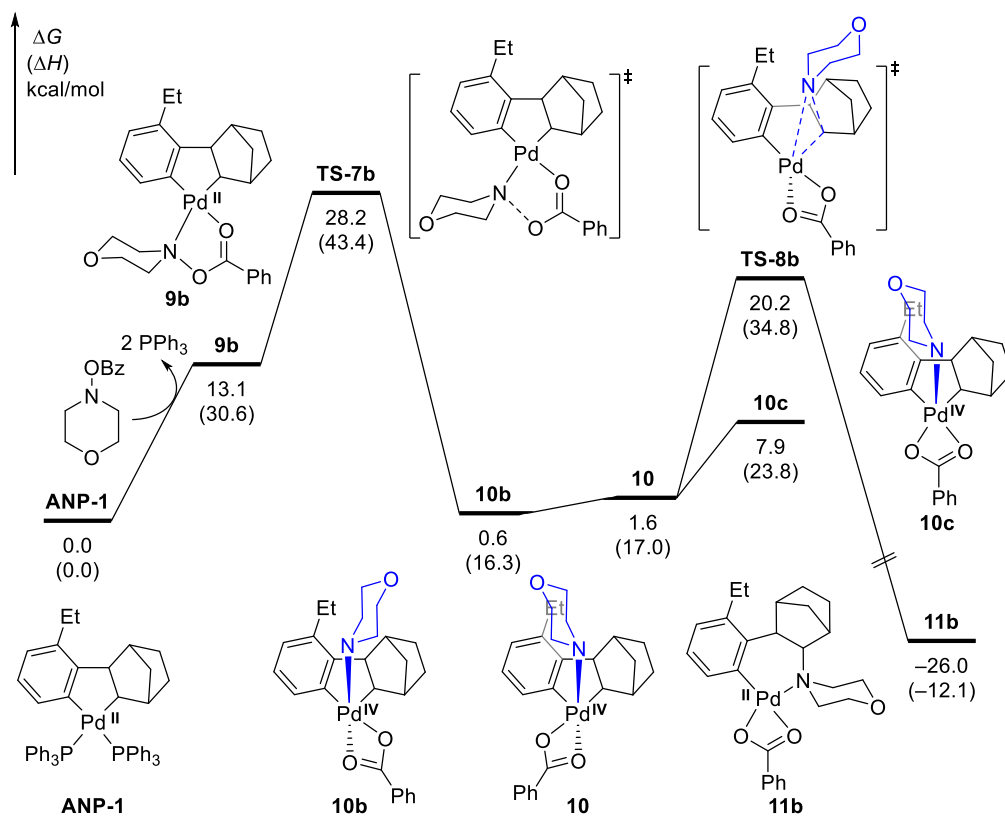


Fig. S4 Disfavored reaction pathway of ANP-1 oxidation with EY-1 through concerted oxidative addition mechanism.

As shown in Fig. S5, **TS-6b** was located as another possibility of the S_N2 -type oxidative addition to ANP-1. The relative free energy of **TS-6b** is higher than that of **TS-6** (Fig. 3a) by 4.5 kcal/mol, which could be attributed to the increased steric repulsion of PPh_3 with the norbornyl group. From ANP-2c, a five-membered cyclic transition state **TS-4b** for the concerted oxidative addition mechanism was located. This transition state has a higher free energy than that of **TS-4** by 2.0 kcal/mol. For the C–N reductive elimination from Pd(IV) complexes **6b** and **6**, transition state **TS-5c** was located for the $C(sp^2)$ –N reductive elimination, and **TS-5d** and **TS-5a** were located for the $C(sp^2)$ –N reductive elimination. These transition states are disfavored compared with **TS-5** (Fig. 3a) because of the higher free energies.

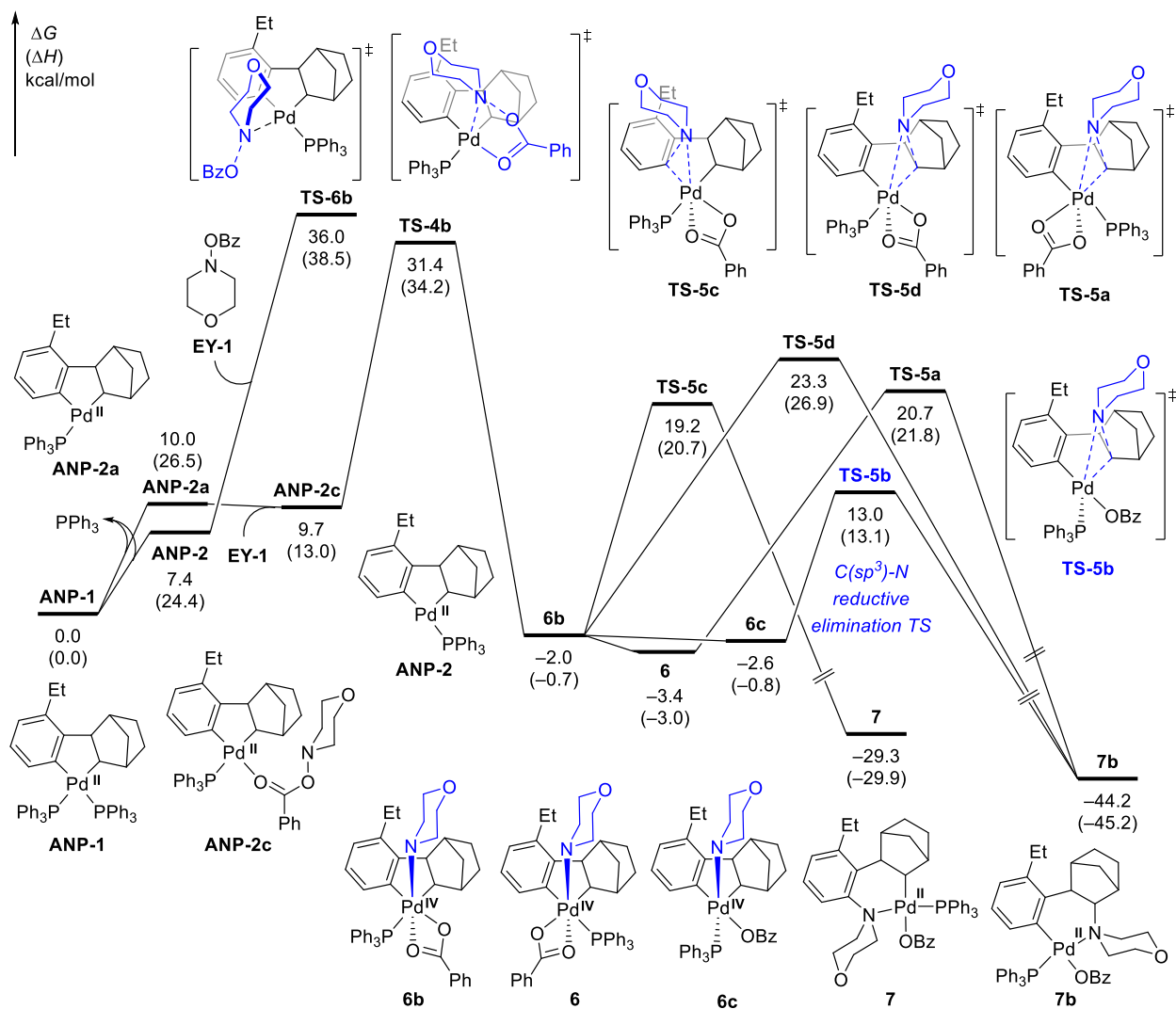


Fig. S5 Disfavored reaction pathways of neutral ANP oxidation through concerted and S_N2-type oxidative addition mechanism.

5. Disfavored reaction pathways of the oxidation of iodide-bound anionic ANP with EY-1

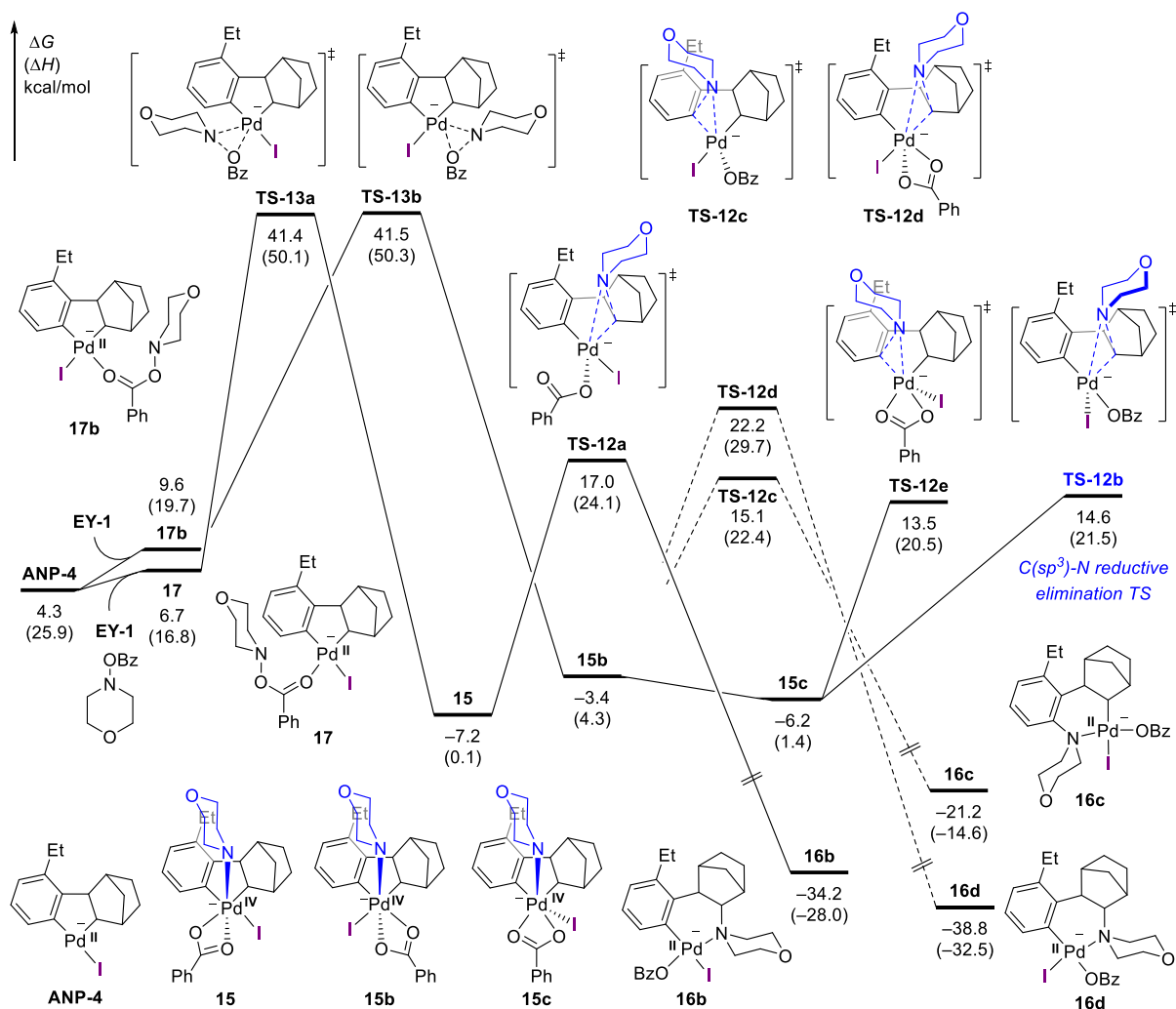


Fig. S6 Disfavored reaction pathways of ANP-4 oxidation through three-membered cyclic oxidative addition transition states.

For the oxidative addition of EY-1 to ANP-4, both the five-membered and three-membered cyclic transition states were studied in this work. Fig. S6 shows two three-membered cyclic transition states **TS-13a** and **TS-13b**. These two transition states have comparable activation free energies, which are much higher than that of five-membered cyclic transition state **TS-13** (Fig. 3b). Therefore, the ANP-4 oxidation through three-membered cyclic oxidative addition transition state is disfavored. The energy difference could be ascribed to the prominent ring strain in **TS-13a** and **TS-13b**. In addition, several C–N reductive elimination transition states from different Pd(IV) complexes were located. These transition states all have higher activation free energies than **TS-**

12 (Fig. 3b).

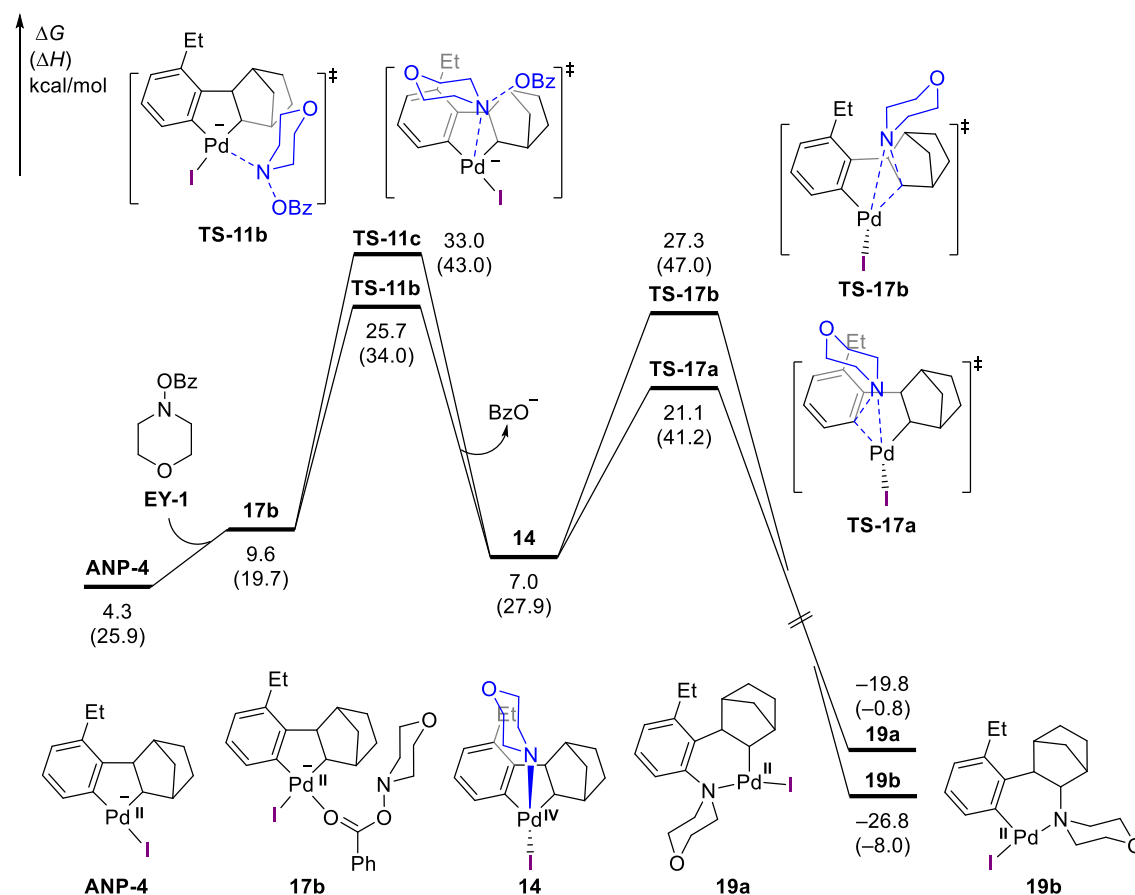


Fig. S7 Disfavored reaction pathways of ANP-4 oxidation through S_N2-type oxidative addition mechanism.

Besides the cyclic oxidative addition transition states, several possible S_N2-type oxidative addition transition states have also been considered. As shown in Fig. S7, S_N2-type oxidative addition transition states **TS-11b** and **TS-11c** were located for the oxidation of ANP-4 with EY-1. In **TS-11b**, the electrophile approaches the metal center at the *trans* position to the sp² carbon, and in **TS-11c**, the electrophile is at the apical position of Pd. While in the most favorable transition state **TS-11** (Fig. 3b), the electrophile is at the *trans* position to the sp³ carbon. The stronger *trans* effect of the alkyl group is responsible for the lower activation free energy. After the oxidation of ANP-4, a neutral Pd(IV) complex **14** is formed with the release of BzO⁻. Subsequent C(sp²)-N and C(sp³)-N reductive elimination could occur through transition states **TS-17a** and **TS-17b**, respectively. The formation of C(sp²)-N bond via **TS-17a** is kinetically favored by 6.2 kcal/mol.

However, the relative free energy of **TS-17a** is 14.0 kcal/mol higher than that of **TS-12** (Fig. 3b) because the unsaturated coordination of Pd in **14** makes it less stable than the BzO^- -coordinated Pd(IV) intermediate **15** (Fig. 3b).

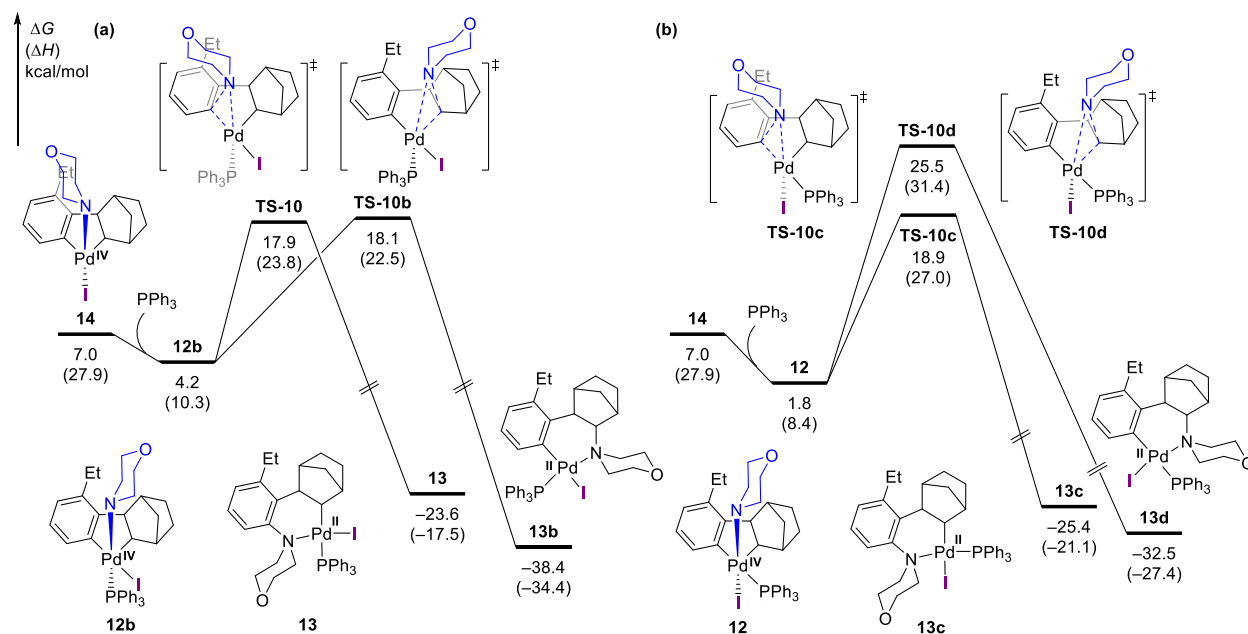


Fig. S8 Disfavored reaction pathways of C–N reductive elimination from Pd(IV) complexes.

The C–N reductive elimination with the coordination of PPh_3 to **14** was also studied. As shown in Fig. S8, the coordination of PPh_3 to **14** could lead to the formation of neutral ANP complexes **12b** or **12**. From complex **12b**, $\text{C}(\text{sp}^2)$ –N and $\text{C}(\text{sp}^3)$ –N reductive elimination could occur through transition states **TS-10** and **TS-10b**, respectively. From complex **12**, the $\text{C}(\text{sp}^2)$ –N and $\text{C}(\text{sp}^3)$ –N reductive elimination could occur through transition states **TS-10c** and **TS-10d**, respectively. The computational results suggest that the $\text{C}(\text{sp}^2)$ –N bond formation is always favored over the $\text{C}(\text{sp}^3)$ –N formation. The C–N reductive elimination from neutral ANP complexes is less favored than that from the anionic ANP complex **15** due to the relatively high free energy of **12b** and **12**. Therefore, the coordination of anionic ligand to Pd(IV) not only stabilizes the ANP complex but also promote the C–N reductive elimination.

6. Reaction pathways of the oxidation of the BzO⁻-bound anionic ANP with EY-1

The coordination of an anionic ligand to the ANP complex is critical for ANP oxidation and C–N bond formation. In addition to iodide anion, BzO⁻ could also coordinate with the metal center and form a new anionic ANP complex **ANP-6** (Fig. S9). The oxidative addition of **EY-1** to **ANP-6** could occur through concerted or S_N2-type mechanism. Computational results of concerted oxidative addition pathway and subsequent C–N bond formation are shown in Fig. S9. Two three-membered cyclic transition states **TS-18a** and **TS-18b** have extremely high activation free energies. All attempts toward locating the five-membered cyclic transition states with **ANP-6** have failed. Such five-membered cyclic OA transition state, if exists, is expected to be disfavored, because the structurally similar five-membered OA transition state **TS-13** with **ANP-4** has a higher energy barrier than the corresponding S_N2-type transition state **TS-11**. The following C(sp²)–N and C(sp³)–N bond formation occurs through C–N reductive elimination transition states **TS-19a** and **TS-19b**, respectively. The formation of C(sp²)–N bond is favored. However, considering the high activation free energies of **TS-18a** and **TS-18b**, the concerted oxidative addition mechanism is less likely for **ANP-6** oxidation.

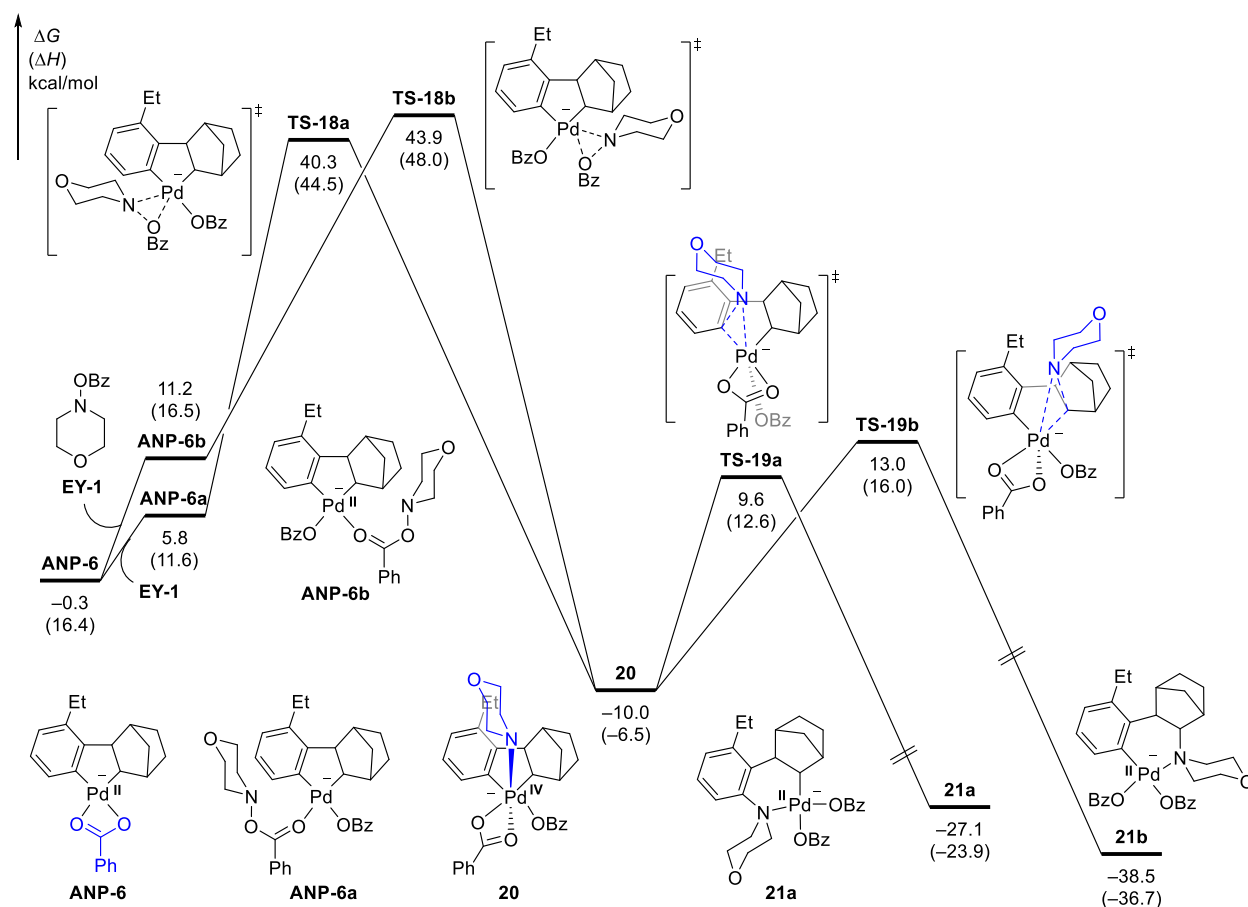


Fig. S9 Reaction pathways of the ANP-6 oxidation through concerted oxidative addition mechanism and the subsequent C–N bond formation.

In the S_N2 -type oxidative addition pathway with ANP-6, three transition states (TS-20, TS-20a, and TS-20b) were located (Fig. S10). Among them, TS-20 is less favored because EY-1 is at the sterically more hindered apical site of the ANP. TS-20a and TS-20b have comparable activation free energies, which are much smaller than that of TS-18a (Fig. S9). Subsequent $C(sp^2)$ –N reductive elimination through TS-5b with an activation free energy of 15.6 kcal/mol is relatively facile. Therefore, the ANP-6 oxidation with morpholino benzoate (EY-1) prefers to occur through the S_N2 -type oxidative addition mechanism.

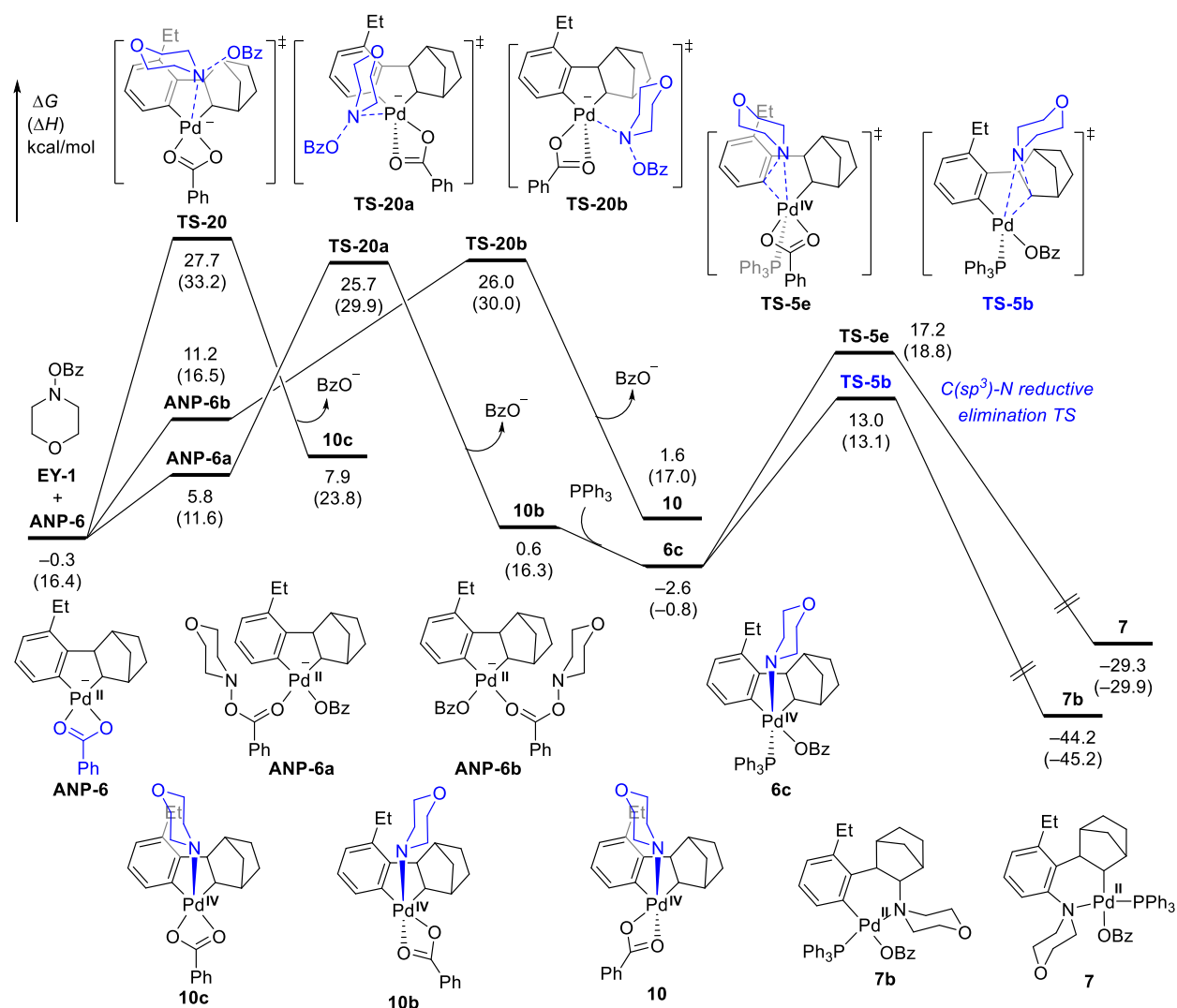


Fig. S10 Reaction pathways of the ANP-6 oxidation through the S_N2-type mechanism and the subsequent C–N bond formation.

The effect of PPh₃ coordination on ANP-6 oxidation was also studied in this work. As shown in Fig. S11, ANP-5 and ANP-5b could be formed through the coordination of PPh₃ to ANP-6. The oxidative addition of EY-1 to ANP-5 or ANP-5b occurs through the S_N2-type transition states TS-21 and TS-21b, respectively. Because the electrophile is at the apical site of ANP, which is sterically more hindered, the activation free energy of TS-21b is found to be higher than that of TS-20a or TS-20b. Therefore, the coordination of PPh₃ to the anionic ANP species is disfavored in the ANP oxidation.

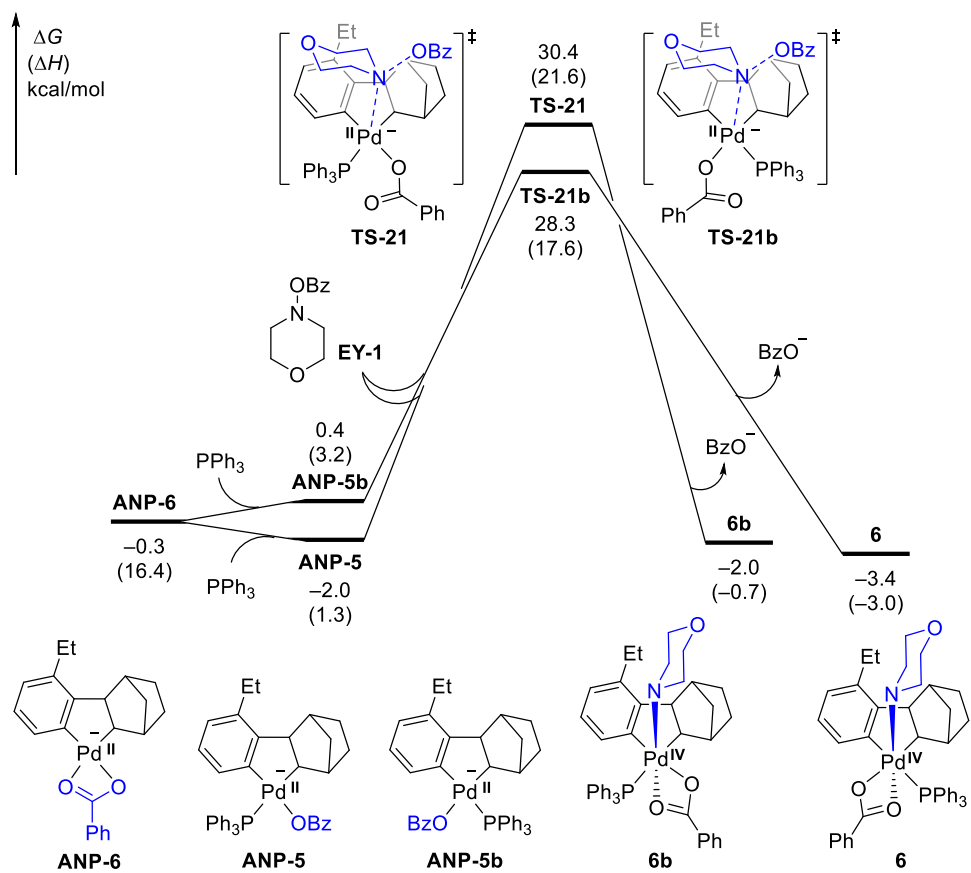
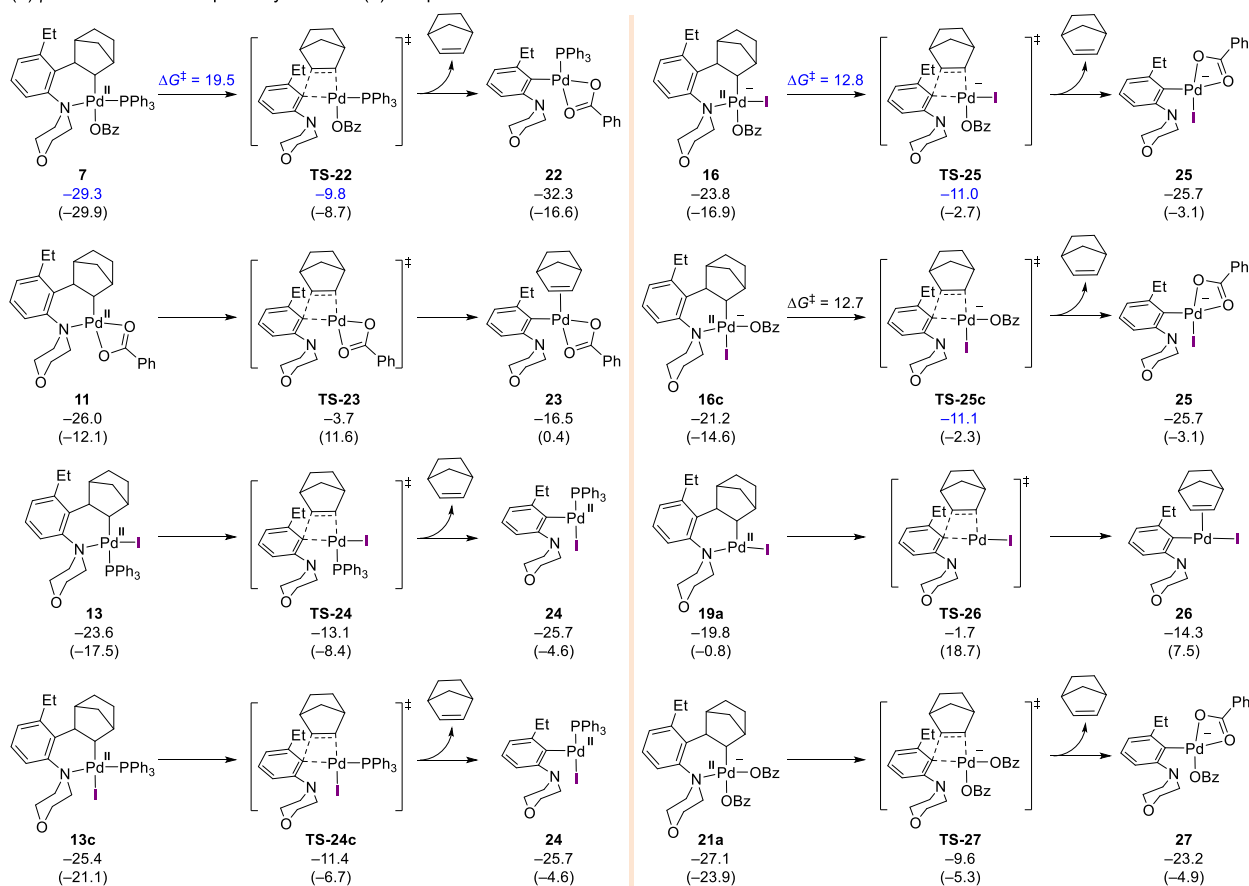


Fig. S11 Reaction pathways of the ANP-5 and ANP-5b oxidation through the S_N2-type mechanism.

7. Reaction pathways of β -carbon elimination and hydride transfer from Pd(II) complexes

(a) β -carbon elimination pathways from Pd(II) complexes



(b) Hydride transfer pathways from neutral and anionic Pd(II) species

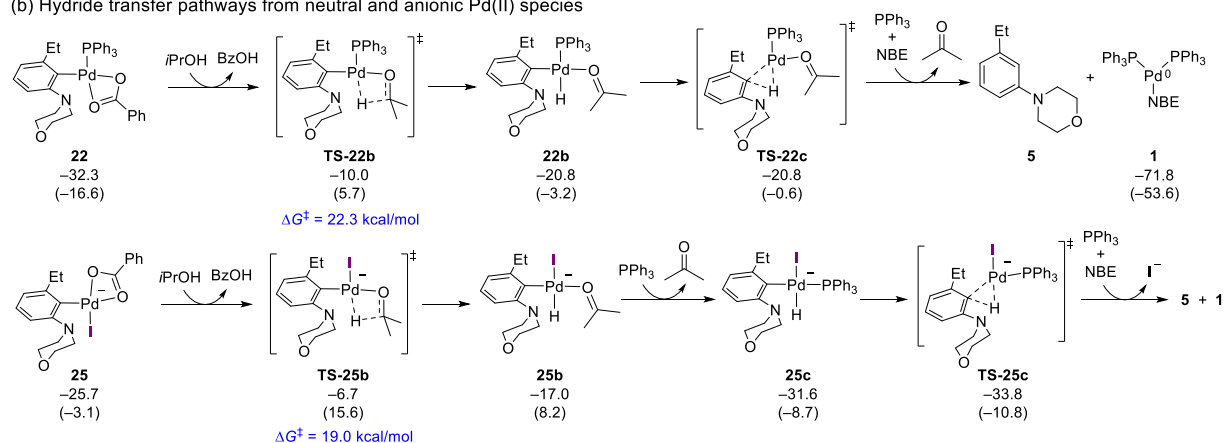


Fig. S12 Calculated reaction pathways of β -carbon elimination and hydride transfer from various Pd(II) complexes. All energies are in kcal/mol.

In Pd/NBE cooperative catalysis, β -carbon elimination and hydride transfer will occur after

the C(sp²)-N reductive elimination. The possible β -carbon elimination transition states from various Pd(II) complexes were calculated and summarized in Fig. S12a. The activation free energies are generally lower than the rate-determining ANP-4 oxidation. Our computational results reveal that the most favored ANP oxidation pathway followed by C(sp²)-N reductive elimination leads to the formation of anionic Pd(II) complex **16**. The corresponding β -carbon elimination from **16** could take place through **TS-25** with an activation free energy of 12.8 kcal/mol. This energy barrier is 9.1 kcal/mol lower than that of ANP-4 oxidation (Fig. 3). From neutral Pd(II) complex, the most stable β -carbon elimination transition state **TS-22** has an activation free energy of 19.5 kcal/mol.

Subsequent hydride transfer from neutral Pd(II) complex **22** occurs through β -H elimination transition state **TS-22b** and C-H reductive elimination transition state **TS-22c**. Thus, the activation free energies for hydride transfer from **22** is 22.3 kcal/mol, which is 5.5 kcal/mol lower than that of ANP-1 oxidation via **TS-7** (Fig. 3). The analogous process from anionic Pd(II) complex **25** could occur through β -H elimination transition state **TS-25b** and C-H reductive elimination transition state **TS-25c**. The activation free energy is 19.0 kcal/mol, which is 2.9 kcal/mol lower than that of ANP-4 oxidation via **TS-11** (Fig. 3). Therefore, both the β -carbon elimination and hydride transfer are relatively facile compared with the ANP oxidation step.

8. Activation free energies of C–C reductive elimination from various ANP complexes

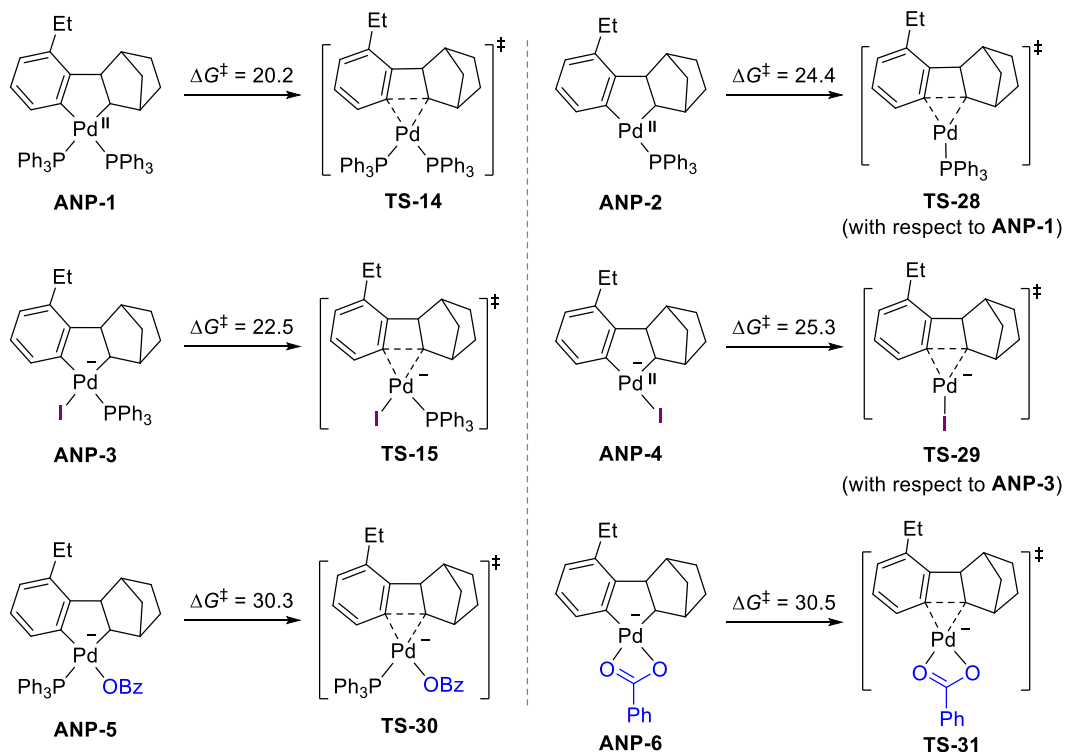


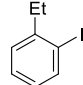
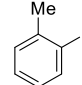
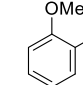
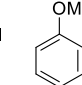
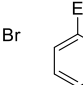
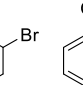
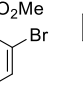
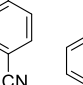
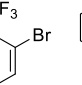
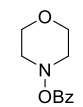
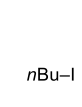
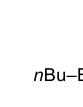
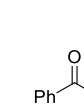
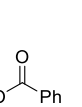
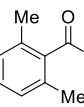
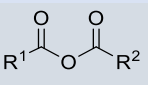
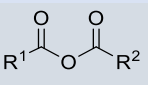
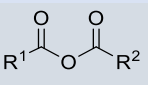
Fig. S13 Calculated activation free energies of C–C reductive elimination from various ANP complexes. All activation free energies are in kcal/mol with respect to corresponding ANP complexes unless otherwise noted.

The C–C reductive elimination from ANP complex is a potential side-reaction in Pd/NBE cooperative catalysis. The C–C reductive elimination from various three- and four-coordinated ANP complexes supported by phosphine or anionic ligands have been studied using DFT calculations. As shown in Fig. S13, computational results suggested that the neutral ANP species, especially two phosphine ligands coordinated ANP species, have a lower energy barrier to the C–C reductive elimination. While the anionic ligand coordinated ANP species have relatively high activation free energies of C–C reductive elimination. The computational study of anion effects suggests that the ANP species with anionic ligand coordination is most likely the active species for ANP oxidation.

9. Concerted and S_N2-type oxidative addition transition states of Pd(0) and ANP-4 oxidation with various Ar–X and E–Y

A series of Ar–X and E–Y were investigated to study the possible oxidative addition mechanisms and the orthogonal reactivity of electrophiles. The Ar–X investigated here include ArX-1, ArX-2, ArX-3, ArX-4, and ArX-5; and the E–Y include EY-1, EY-2, EY-3, EY-4, EY-5, EY-6, EY-7, EY-8, EY-9, and EY-10. The oxidative addition transition states of different electrophiles to Pd(0) complex (**1**) and ANP-4 are summarized in Figs. S14, S15, and S16. To reveal the most favorable reaction mechanism of different electrophiles with Pd(0) and Pd(II) species, we compared the computed activation energies of the concerted cyclic oxidative addition (via either three- or five-centered transition states) and S_N2-type oxidative addition transition states. These results are summarized in Table S1.

Table S1. The most favorable oxidative addition mechanisms in reactions of Pd0 and ANP-4 with various electrophiles.

																				
ArX-1	ArX-2	ArX-3	ArX-4	ArX-5	EY-4	EY-5	EY-8	EY-9												
																				
EY-1	EY-2	EY-7	EY-3	EY-6	EY-10															
						<table border="1"> <thead> <tr> <th></th> <th>Pd0</th> <th>ANP-4</th> </tr> </thead> <tbody> <tr> <td>E(sp³)-Y (EY-1, 2, 7)</td> <td>S_N2-type</td> <td>S_N2-type</td> </tr> <tr> <td>E(sp²)-Y (ArX-1~5 & EY-4, 5, 8, 9)</td> <td>Three-centered</td> <td>Three-centered</td> </tr> <tr> <td> (EY-3, 6, 10)</td> <td>Three-centered</td> <td>Five-centered</td> </tr> </tbody> </table>				Pd0	ANP-4	E(sp³)-Y (EY-1, 2, 7)	S _N 2-type	S _N 2-type	E(sp²)-Y (ArX-1~5 & EY-4, 5, 8, 9)	Three-centered	Three-centered	 (EY-3, 6, 10)	Three-centered	Five-centered
	Pd0	ANP-4																		
E(sp³)-Y (EY-1, 2, 7)	S _N 2-type	S _N 2-type																		
E(sp²)-Y (ArX-1~5 & EY-4, 5, 8, 9)	Three-centered	Three-centered																		
 (EY-3, 6, 10)	Three-centered	Five-centered																		

The computational results suggested that the E(sp³)-Y type electrophiles (**EY-1, 2, 7**), which have an sp³ hybridized electrophilic center, prefer the S_N2-type oxidative addition transition state; while the E(sp²)-Y type oxidants (including aryl halides), which have an sp² hybridized

electrophilic center, prefer to react with Pd catalyst through the cyclic transition state (Table S1). It should be noted that the oxidative addition of **EY-3** to **ANP-4** occurs through the five-centered TS while the OA to **Pd(0)** prefers the three-centered TS. The five-centered OA TS with Pd(PPh₃)₂, in which the carbonyl group on **EY-3** is coordinated to the Pd, is disfavored because the Pd(0) is more electron-rich and the large P–Pd–P angle (117.3° in **TS-40**) prevents the more sterically encumbered five-centered TS. After dissociation of one of PPh₃ ligands, a five-centered transition state (**TS-40b**) could be located. However, this mono-phosphine ligated five-centered TS is less stable by 1.6 kcal/mol than **TS-40**.

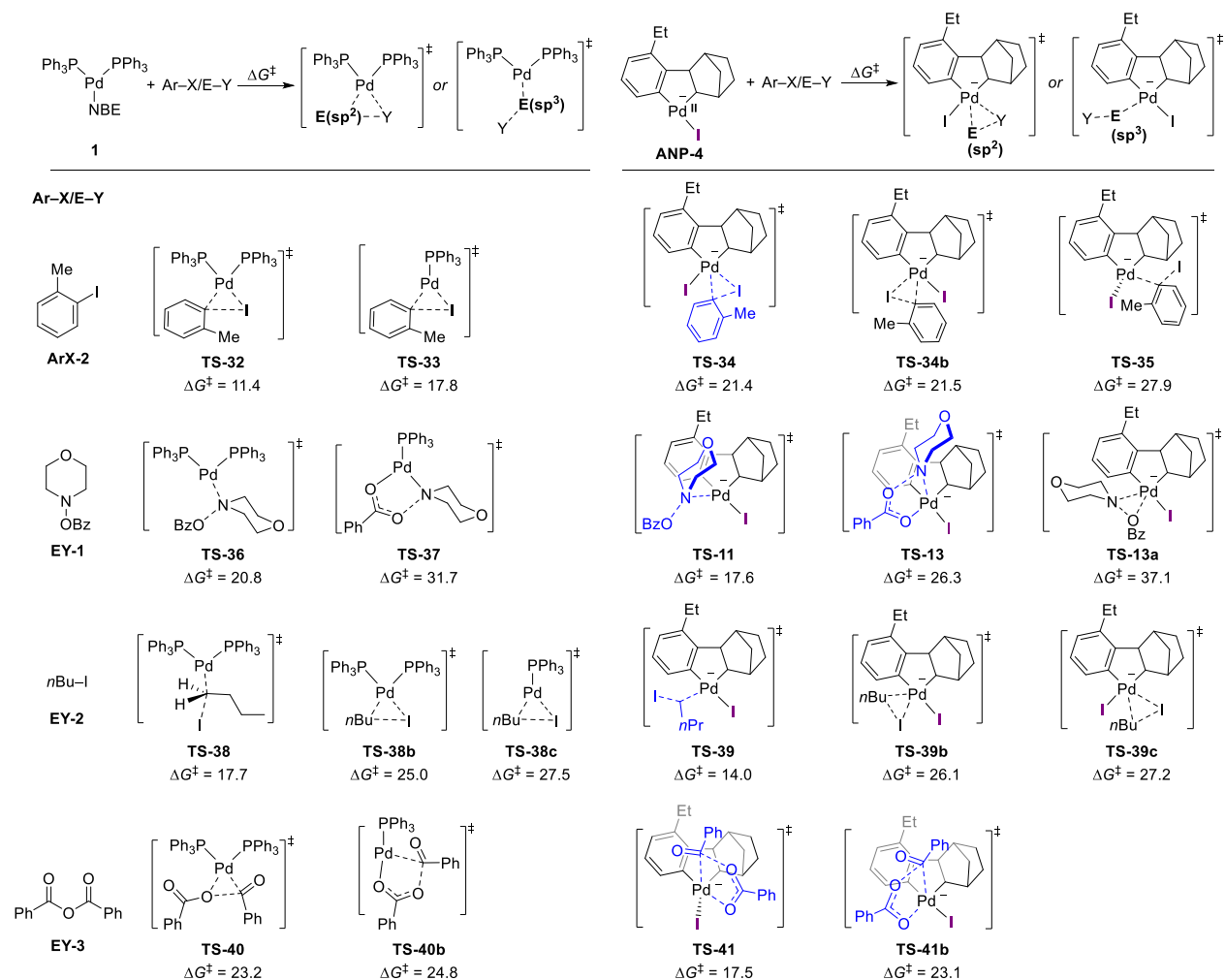


Fig. S14 Concerted and S_N2-type oxidative addition transition states of **Pd(0)** and **ANP-4** oxidation with **ArX-2**, **EY-1**, **EY-2**, and **EY-3**. All energies are in kcal/mol.

The oxidation of Pd(0) complex **1** or **ANP-4** with morpholino benzoate, alkyl iodide, and alkyl bromide (**EY-1**, **2**, **7**), always prefers to occur through the S_N2-type oxidative addition

mechanism (Fig. S14 and S16). The concerted mechanism is disfavored here due to the lack of stabilizing $d \rightarrow \pi^*$ back-donation between Pd and $E(sp^3)-Y$ in the cyclic transition state, which could lead to the decrease of interaction energy. Moreover, the preference of $E(sp^3)-Y$ electrophiles to S_N2 -type oxidative mechanism is also related to the weak bond dissociation energy (BDE, see Fig. S24 for the BDE values). These features all promote the outer-sphere cleavage of the $E(sp^3)-Y$ bond.

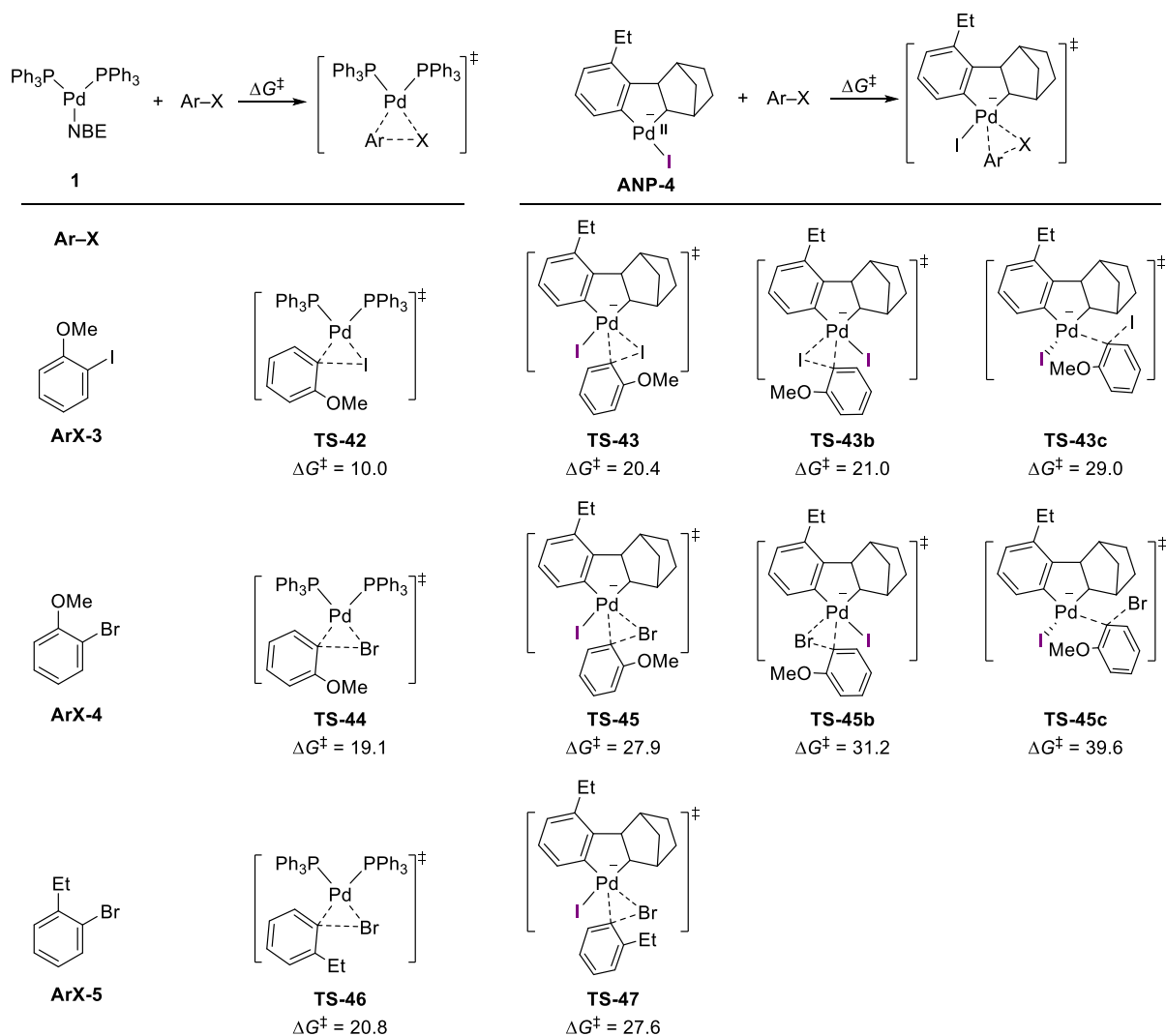


Fig. S15 Concerted oxidative addition transition states of **Pd(0)** and **ANP-4** oxidation with **ArX-3**, **ArX-4**, and **ArX-5**. All energies are in kcal/mol.

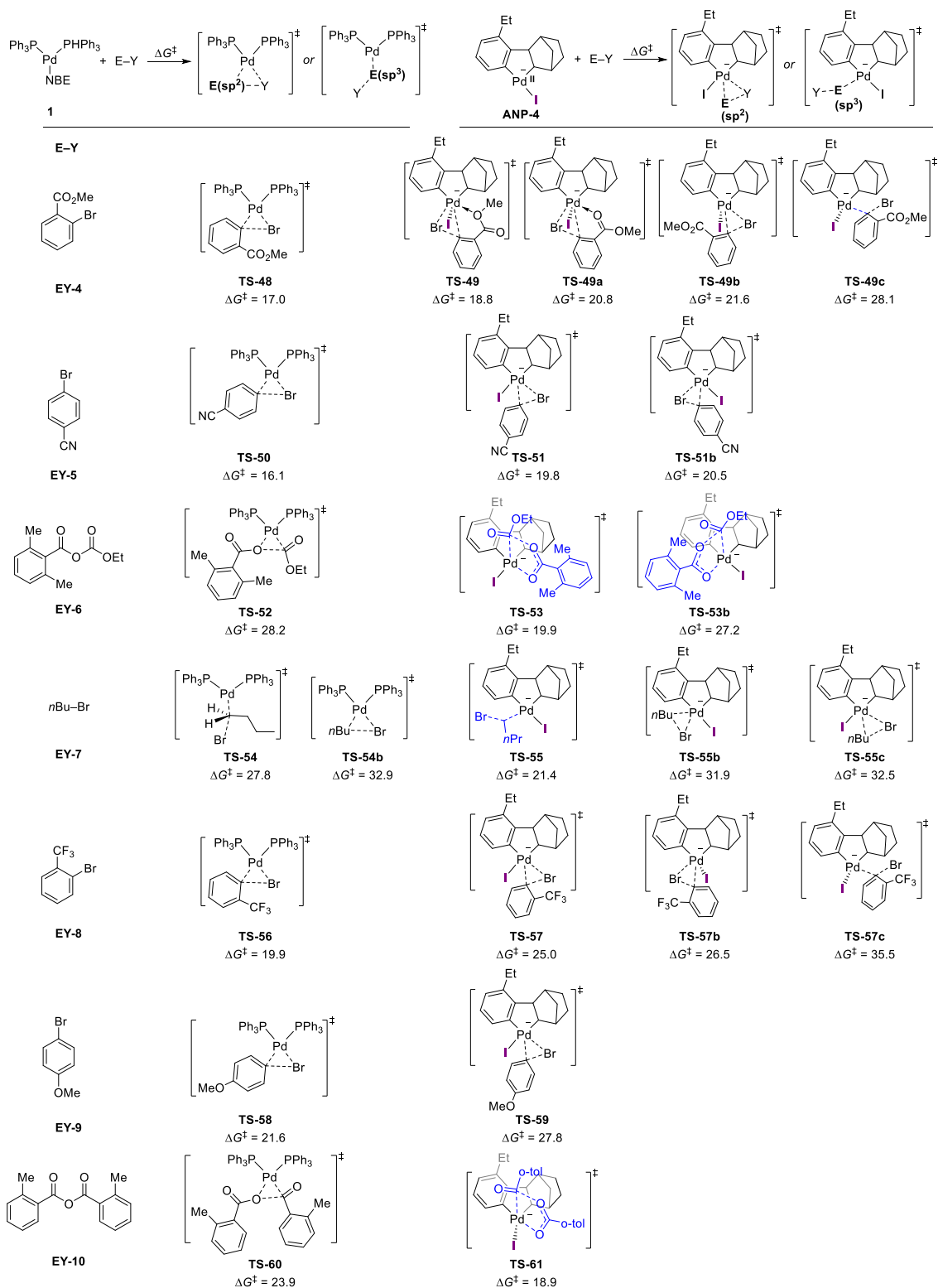


Fig. S16 Concerted and $\text{S}_{\text{N}}2$ -type oxidative addition transition states of $\text{Pd}(0)$ and ANP-4 oxidation with EY-4~10. All energies are in kcal/mol.

It is noteworthy that the exclusive chelation of the *ortho*-ester group with the Pd(II) center of ANP is observed in **TS-49** (Fig. S16). This chelating effect is supposed to promote the oxidative addition of **EY-4** to **ANP-4** by stabilizing the cyclic transition state. The chelation of the *ortho*-ester group with Pd(0) center is not found in the cyclic transition state **TS-48**. It could be attributed to the lack of available coordination sites in the four-coordinated transition state. With the computed activation free energies of various aryl halides (Ar-X) to **Pd0** and **ANP-4**, the comparison among different Ar-X is shown in Fig. S17. The Ar-X are listed in ascending order according to $\Delta G^\ddagger(\text{Pd0}+\text{ArX})$. Compared with aryl iodides, aryl bromides (**ArX-4** and **ArX-5**) have higher energy barriers to the oxidation of Pd(0) and Pd(II). The lower reactivity of aryl bromide could be attributed to the higher BDE of the C-Br bond (Fig. S24).

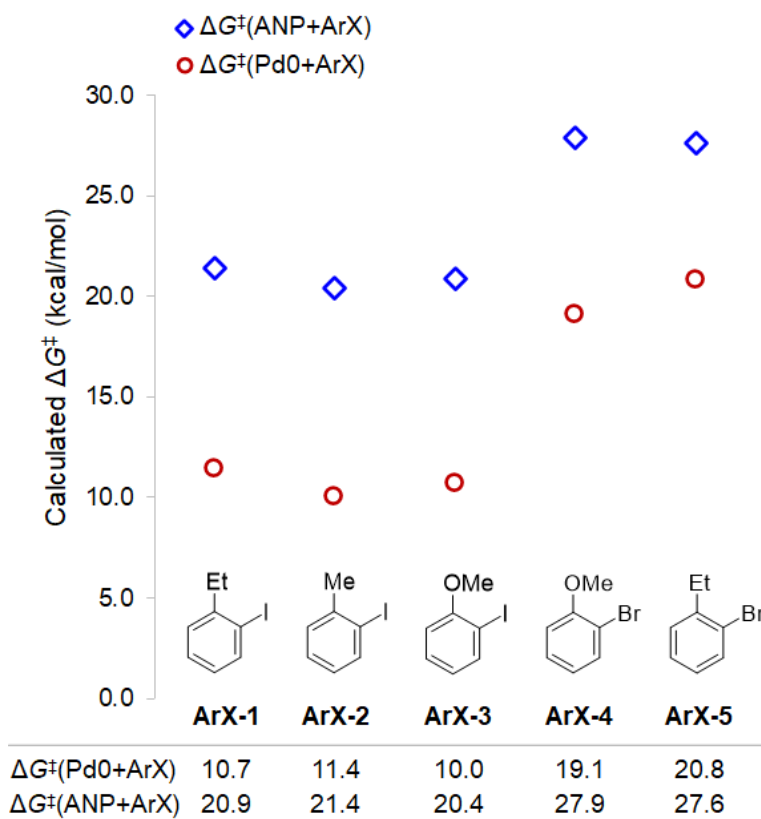


Fig. S17 Comparison of the reactivity of various aryl halides (Ar-X) to **Pd0** and **ANP-4**. All energies are in kcal/mol.

10. Concerted oxidative addition and S_N2-type transition states of BzO⁻-bound anionic ANP

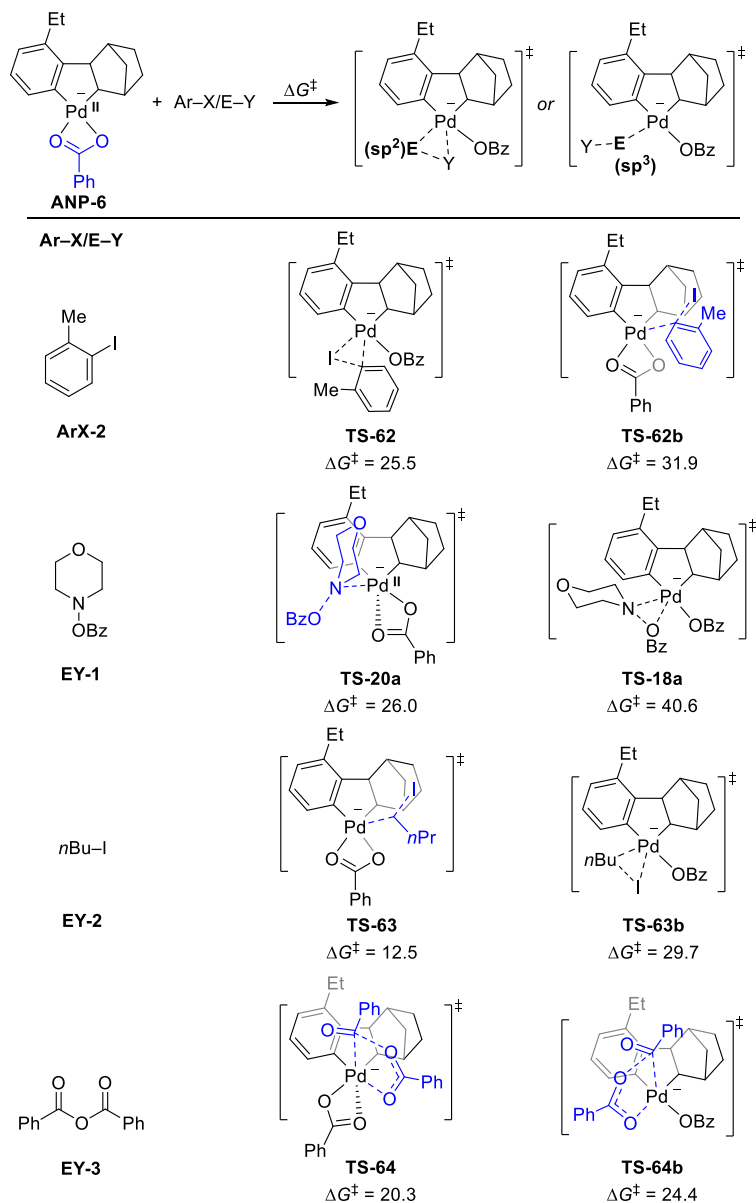


Fig. S18 Concerted and S_N2-type oxidative addition transition states of BzO⁻-bound anionic ANP (**ANP-6**) oxidation with representative Ar-X and E-Y. All energies are in kcal/mol.

The oxidative addition of electrophiles to BzO⁻-bound anionic ANP species **ANP-6** has been calculated to get the most stable transition state for a given electrophile. Four representative electrophiles, including aryl iodide **ArX-2**, morpholino benzoate **EY-1**, 1-iodobutane **EY-2**, and anhydride **EY-3**, are employed in calculation (Fig. S18). **ANP-6** has the analogous reactivity as

the iodide-bound anionic ANP complex **ANP-4**. The oxidation of **ANP-6** with aryl iodide **ArX-2** still prefers the three-membered cyclic transition state over the S_N2 -type transition state, while the reactions with morpholino benzoate and alkyl iodide favor the S_N2 -type transition state. Moreover, the oxidative addition of anhydride always prefers the five-membered cyclic transition state. Therefore, the most favored oxidative addition mechanism for the electrophile with **ANP-6** remains the same as that with **ANP-4**.

11. Optimized structures of oxidative addition transition states and distortion-interaction analysis

We performed natural population analysis (NPA) charge calculations and distortion/interaction analysis to understand why the neutral and anionic ANP complexes prefer different OA mechanisms and to explore the origin of the higher reactivity of the anionic ANP complex in the S_N2 -type OA pathway (Fig. S19). A substantial amount of charge transfer from the ANP complex to the electrophile is observed in the S_N2 -type OA TS. The negatively charged ANP complex (**ANP-4**) promotes such charge transfer ($0.70e$ in **TS-11** versus $0.33e$ in **TS-6**) and thus facilitates the benzoate anion dissociation via the heterolytic cleavage of the N–O bond. The favorable electronic effects that promote the electrophile OA with the anionic ANP complex are further evidenced by the stronger interaction energy ($\Delta E_{\text{int}}^\ddagger$) in **TS-11** than that in **TS-6**. This result indicates that the greater nucleophilicity of the anionic ANP complex promotes the S_N2 -type reaction with electrophile **EY-1**. On the other hand, in the cyclic OA transition states, the anionic ANP interacts less favorably with the electrophile than the neutral ANP complex ($\Delta E_{\text{int}}^\ddagger = -15.6$ and -27.0 kcal/mol in **TS-13** and **TS-4**, respectively). Here, the greater nucleophilicity of the anionic Pd is compensated by the weaker coordination of the carbonyl to the more electron-rich Pd in **TS-13**. As a result, the neutral and anionic ANP complexes have comparable activation

barriers in the cyclic oxidative addition pathways, both of which are higher than **TS-11**. Therefore, the unique electronic property of the electron-rich anionic ANP complex promotes the S_N2 -type OA pathway and increases the reactivity with electrophile **EY-1**.

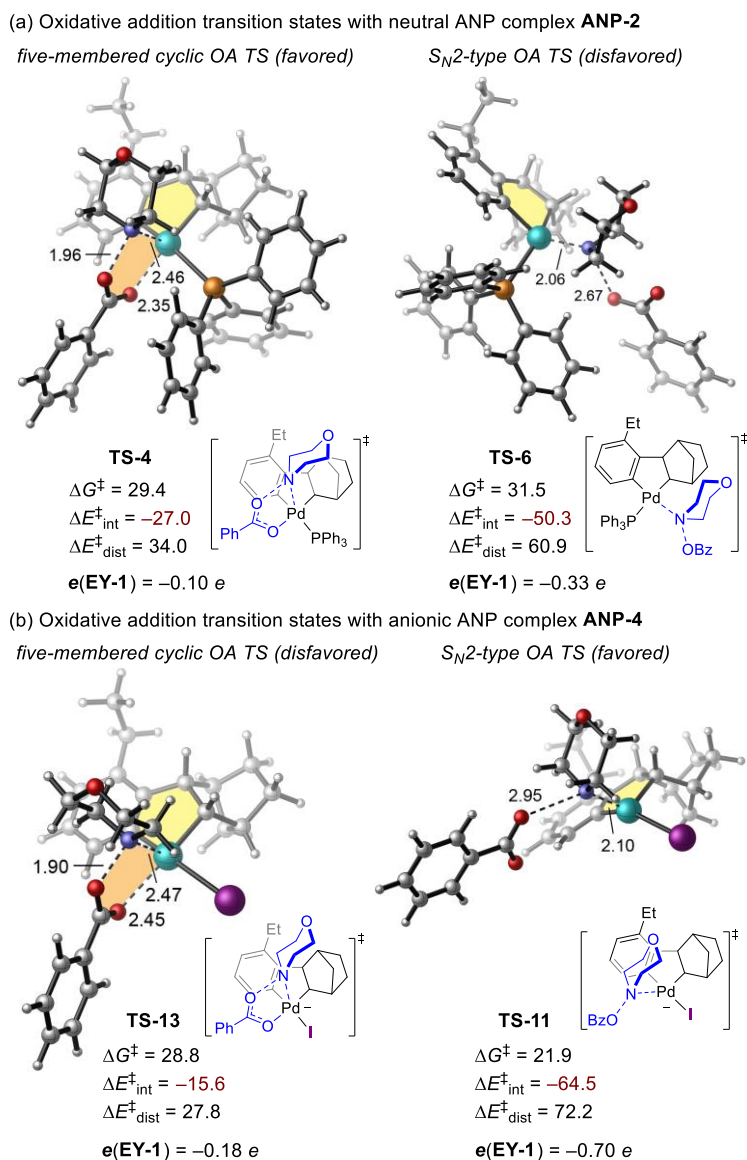


Fig. S19 Origins of the higher reactivity of the S_N2 -type OA with anionic ANP complex **ANP-4**. $e(\text{EY-1})$ is the total NPA charge of **EY-1** in the oxidative addition transition state. $\Delta E_{\text{int}}^\ddagger$ is the interaction energy of the ANP fragment with the electrophile. $\Delta E_{\text{dist}}^\ddagger$ is the sum of the energies to distort the ANP and the electrophile fragments into the transition state geometries. All energies are in kcal/mol.

The optimized structures of cyclic oxidative addition transition states **TS-32** and **TS-34** are shown in Fig. S20. The higher activation free energy of **TS-34** suggests that the oxidation of ANP-4 with 2-iodotoluene (**ArX-1**) is more difficult to occur than the oxidation of Pd(0). The second-order perturbation theory analyses calculated using NBO 3.1 suggest that the stabilizing $d \rightarrow \pi^*$ back-donation in transition state **TS-34** is diminished compared to that in **TS-32** (13.9 kcal/mol). Accordingly, the distortion-interaction analysis revealed that the interaction energy in **TS-34** is less prominent compared with that in **TS-32** (Fig. S20), thereby results in the higher energy barrier to ANP oxidation.

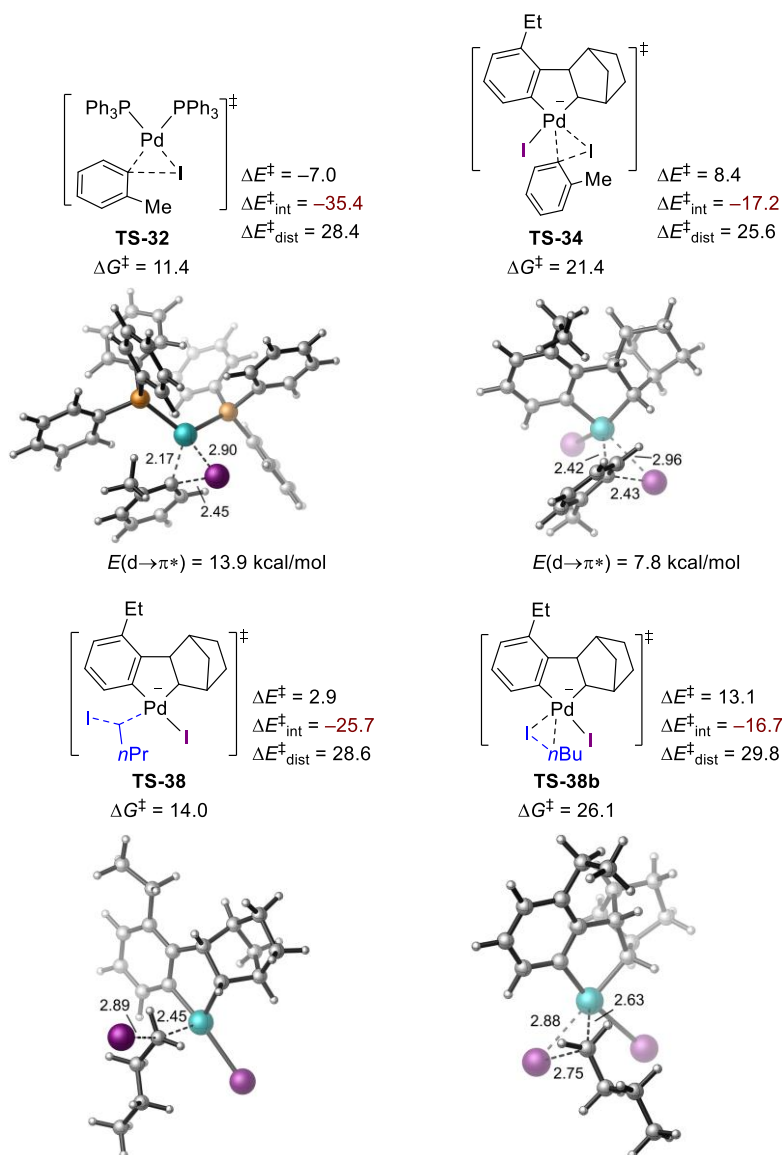


Fig. S20 Optimized structures of oxidative addition transition states with 2-iodotoluene (**ArX-2**) and 1-iodobutane (**EY-2**). All energies are in kcal/mol.

The optimized structures of transition states **TS-38** and **TS-38b** are shown in Fig. S20. These two transition states correspond to the concerted and S_N2-type mechanisms, respectively, for the oxidative addition of 1-iodobutane to **ANP-4**. The distortion-interaction analysis revealed that the alkyl halide involved S_N2-type oxidation transition state **TS-38** has larger interaction energy than that in concerted transition state **TS-38b**. This result is consistent with morpholino benzoate (**EY-1**) involved ANP oxidation. The lower interaction energy in the S_N2-type oxidation transition state makes this mechanism less favored. Besides, the weak BDE of C(sp³)-I bond (61.9 kcal/mol, Fig. S24) also promotes the outer-sphere cleavage of the E(sp³)-Y bond.

Our computational results demonstrate that anhydrides are good electrophiles in ANP oxidation. As shown in Fig. S21, the oxidative addition of **EY-3** to **ANP-4** (via **TS-41**) has a lower energy barrier than that to Pd(0) complex (via **TS-40**). Structural analysis of these two transition states suggests that the more stabilizing five-centered transition state promotes the oxidation of **ANP-4**. Therefore, the anhydride has a higher reactivity with ANP.

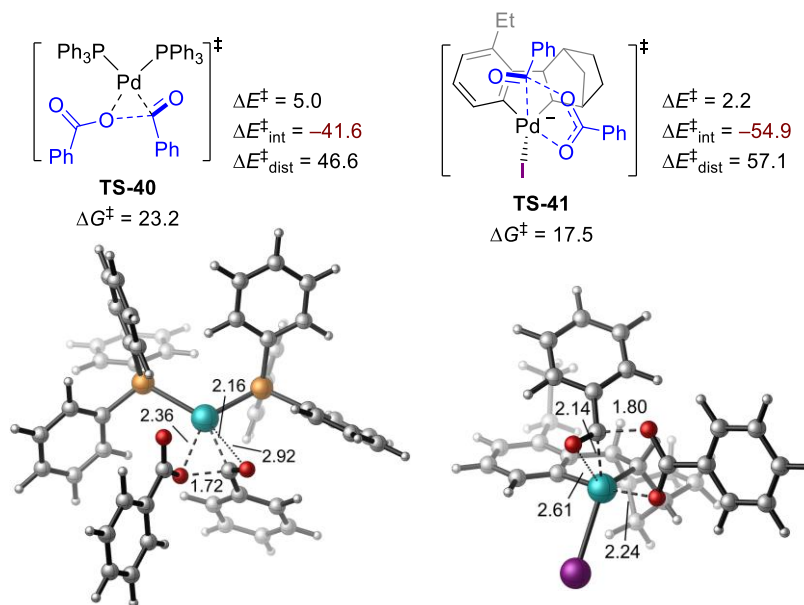


Fig. S21 Optimized structures of oxidative addition transition states with anhydride (**EY-3**). All energies are in kcal/mol.

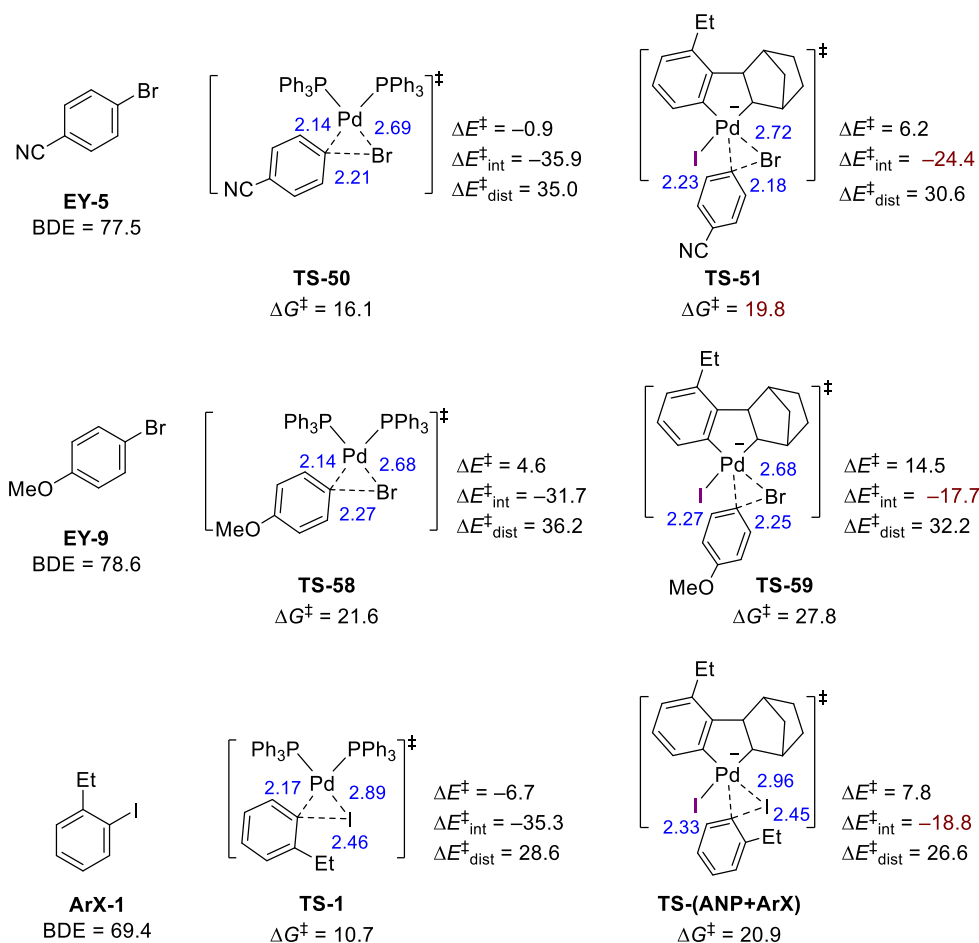


Fig. S22 Activation free energies and distortion-interaction analysis of key Pd oxidation transition states. $\Delta E^\ddagger_{\text{int}}$ is the interaction energy of the Pd/L fragment with the electrophile. $\Delta E^\ddagger_{\text{dist}}$ is the sum of the energies to distort the Pd/L and the electrophile fragments into the transition state geometries. All energies are in kcal/mol. Bond lengths are shown in blue and the unit is angstrom.

Our computational study has demonstrated that electron-deficient Ar-Br (**EY-4** and **EY-5**) have higher reactivity with **ANP-4**, which makes them compatible with a series of Ar-I (**ArX-1**, **ArX-2**, and **ArX-3**) in Pd/NBE cooperative catalysis. In contrast, the electron-rich Ar-Br (**EY-9**) has lower reactivity with **ANP-4** because of the higher activation free energy in ANP oxidation. Distortion-interaction analysis of **ANP-4** oxidation transition states (**TS-51** and **TS-59**) were carried out to compare the reactivity of **EY-5** and **EY-9**. As shown in Fig. S22, **TS-51** has more stabilizing interaction energy than **TS-59** by 6.7 kcal/mol. On the other hand, the energy difference between the Pd(0) oxidative addition with these two aryl bromides (**TS-50** and **TS-58**) is smaller and the interaction energy difference between **TS-50** and **TS-58** is also smaller, which indicate the

oxidative addition to Pd(0) is less sensitive to the electronic effects of Ar–Br than the oxidative addition to ANP-4. These results suggest that the negatively charged Pd(II) center in ANP-4 promotes the $d(\text{Pd}) \rightarrow \pi^*(\text{Ar-Br})$ orbital interactions in the ANP oxidation transition state. The relatively low barrier to the OA of electron-deficient Ar-Br to ANP makes them good electrophiles in the Pd/NBE cooperative catalysis.

12. Comparison between open-shell and closed-shell singlet Pd oxidation transition states

The stability of the DFT wavefunction was tested for all computed structures. Most of the intermediates and transition states are closed-shell singlet (CSS) except for several oxidative addition transition states of EY-1 to ANP (TS-4, TS-6, TS-9, TS-11, TS-13, and TS-37), which are open-shell singlet (OSS). The Mulliken spin densities of these OSS transition states and the energies and structures of the same transition states calculated using closed-shell (restricted) wavefunctions are summarized in Fig. S23. Comparison between results obtained from restricted and broken-symmetry unrestricted calculations revealed that these two types of calculations yielded transition states with similar geometries and comparable energies, which usually differ by a few tenths of a kcal/mol. The Mulliken spin density shows that the benzoate group does not have a radical character in the $\text{S}_{\text{N}}2$ -type transition states. This result and the negative charge of the benzoate group in the TS indicate the benzoate leaving group is dissociated as an anion in the open-shell singlet transition state, which is consistent with the $\text{S}_{\text{N}}2$ -type oxidative addition mechanism. Because the relative free energy of open-shell singlet transition state is slightly lower than that of closed-shell structure, only the open-shell singlet results for these transition states are discussed in the main text. Unless otherwise noted, the alternative $\text{S}_{\text{N}}2$ -type and five-membered cyclic ANP oxidation transition states with EY-1 shown in the Supporting Information are also open-shell singlet (except TS-7 and TS-7b are closed-shell singlet).

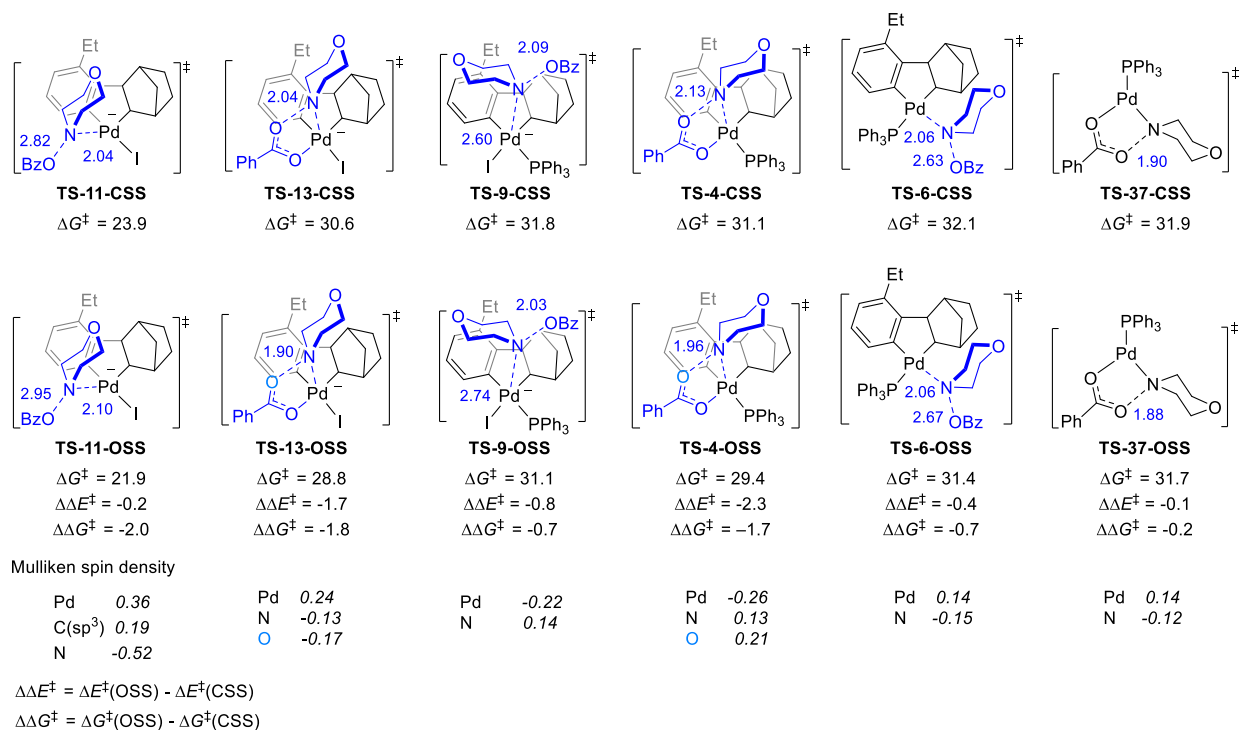


Fig. S23 Comparison between open-shell (OSS) and closed-shell singlet (CSS) transition states. All energies are in kcal/mol. Bond lengths are shown in blue and the unit is angstrom. Mulliken spin densities on certain atoms are shown in italic.

13. Calculated bond dissociation energies (BDE) of Ar–X and E–Y

The bond dissociation energies of each Ar–X and E–Y are calculated at the M06/6-311+G(d,p)–SDD/SMD(toluene)//B3LYP/6-31G(d)–LANL2DZ level of theory. The computational results (Fig. S24) suggest that aryl halides and anhydrides have higher BDE than the alkyl halides and morpholino benzoate, which means E(sp³)–Y type electrophiles have a relatively weak bond for oxidative addition. Therefore, the weak BDE could promote the outer-sphere cleavage of E(sp³)–Y bond during the S_N2-type oxidative addition.

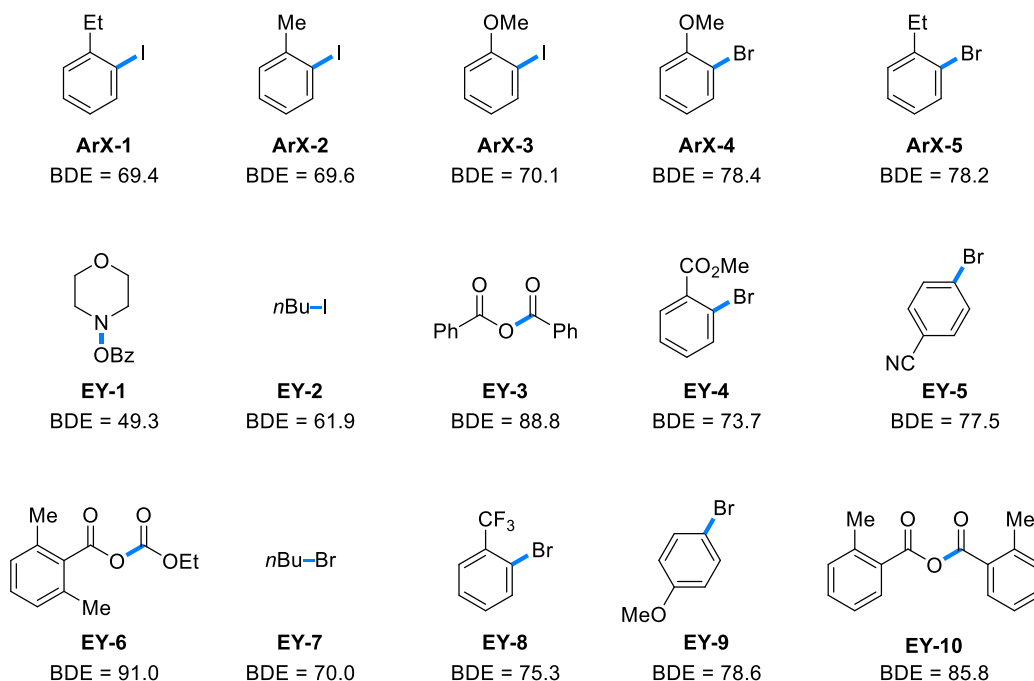


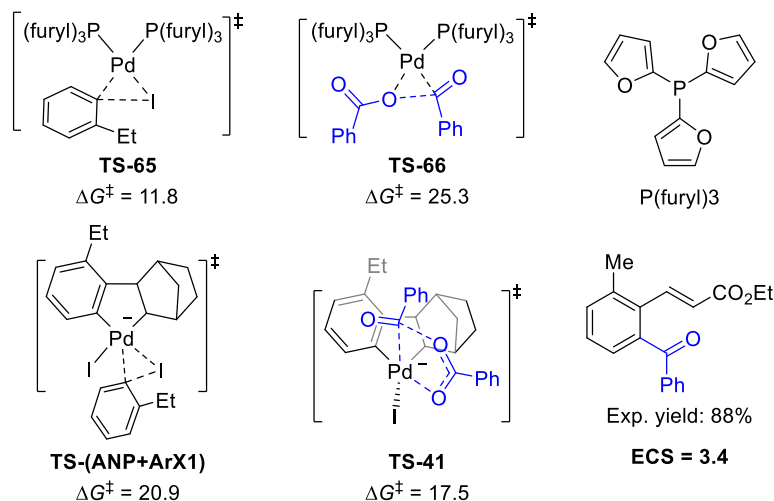
Fig. S24 The bond dissociation energies (BDE) of various Ar–X and E–Y calculated at the M06/6-311+G(d,p)–SDD/SMD(toluene)//B3LYP/6-31G(d)–LANL2DZ level of theory. All energies are in kcal/mol.

14. Calculated ECS of amination and acylation with other electrophiles, aryl halides, and phosphine ligands

In order to validate the reliability of the electrophile compatibility score (ECS) in other Pd/NBE-catalyzed reactions, we have calculated the ECS in several amination and acylation reactions with different hydroxyl amine electrophiles, aryl halides, and phosphine ligands. In these calculations, we evaluated the steric and electronic effects of the aryl halide and the electrophile (Fig. S26 and S27) and the compatibility in the presence with different phosphine ligands (Fig. S25). The computed ECS values were compared with previously reported successful amination and acylation experiments and an unpublished experimental result of an ineffective amination reaction using a bulky N nucleophile (*i*Pr₂N-OBz) (Fig. S28). These new computational and experimental results further support the reliability of ECS on the prediction of electrophile

compatibility in Pd/NBE cooperative catalysis.

a) Electrophile compatibility score (ECS) in Pd/NBE-catalyzed arene acylation with P(furyl)₃



b) Electrophile compatibility score (ECS) in Pd/NBE-catalyzed arene amination with dCypb

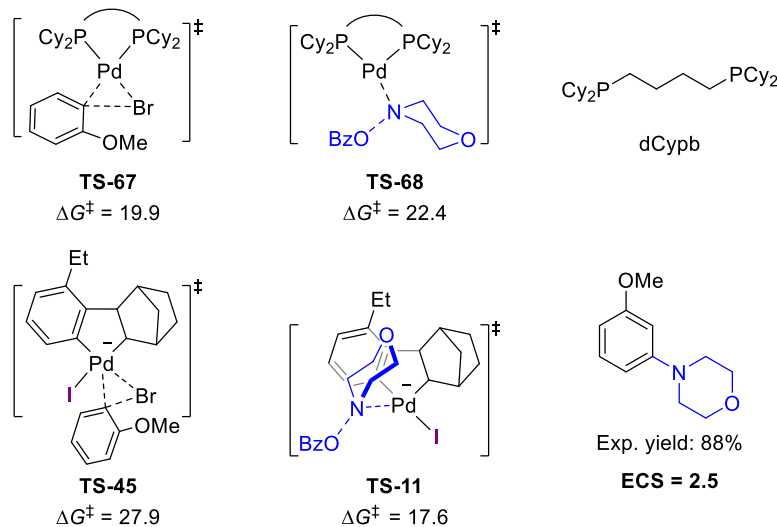


Fig. S25 Calculated electrophile compatibility score (ECS) in Pd/NBE cooperative catalysis with different phosphine ligands.

To confirm whether the electrophile compatibility score (ECS) is applicable to reactions with other phosphine ligands, we calculated the electrophile compatibility scores (ECS) in the Pd/NBE-catalyzed acylation of **ArX-1** with **EY-3** using P(furyl)₃ ligand, and the amination of **ArX-4** with **EY-1** using the dCypb ligand (Fig. S25). The high ECS values suggest both reactions have high compatibility, which is consistent with the high yields observed in previously reported experiment.¹

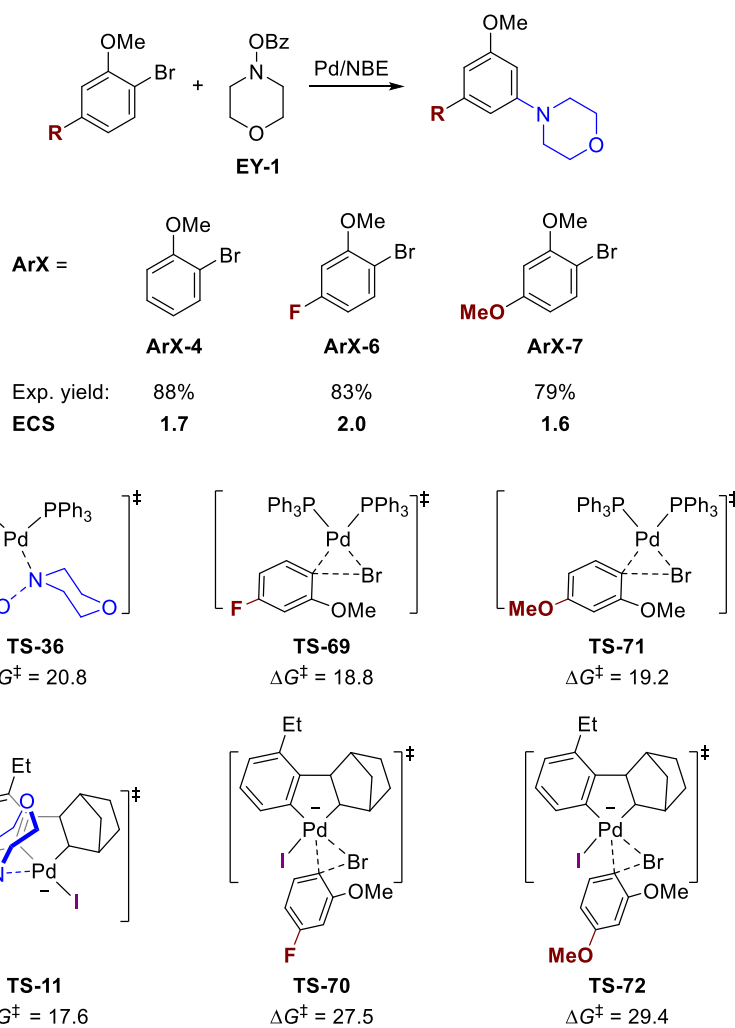


Fig. S26 Calculated electrophile compatibility score (ECS) of trisubstituted aryl bromides with **EY-1** in Pd/NBE-catalyzed arene amination reactions.

To elucidate the electronic effect of aryl halides on the compatibility in arene amination reactions, ECS of two trisubstituted aryl bromides (**ArX-6** and **ArX-7**) with **EY-1** were calculated (Fig. S26). These two new aryl halides have an electron-withdrawing group (-F) and electron-donating group (-OMe), respectively, at the para site of bromide. The ECS values (2.0 and 1.6, respectively) suggest that they are both compatible with **EY-1**. These results are consistent with the high yields of amination products observed in the experiment and indicated a broad substrate scope of aryl halides in the amination reactions.

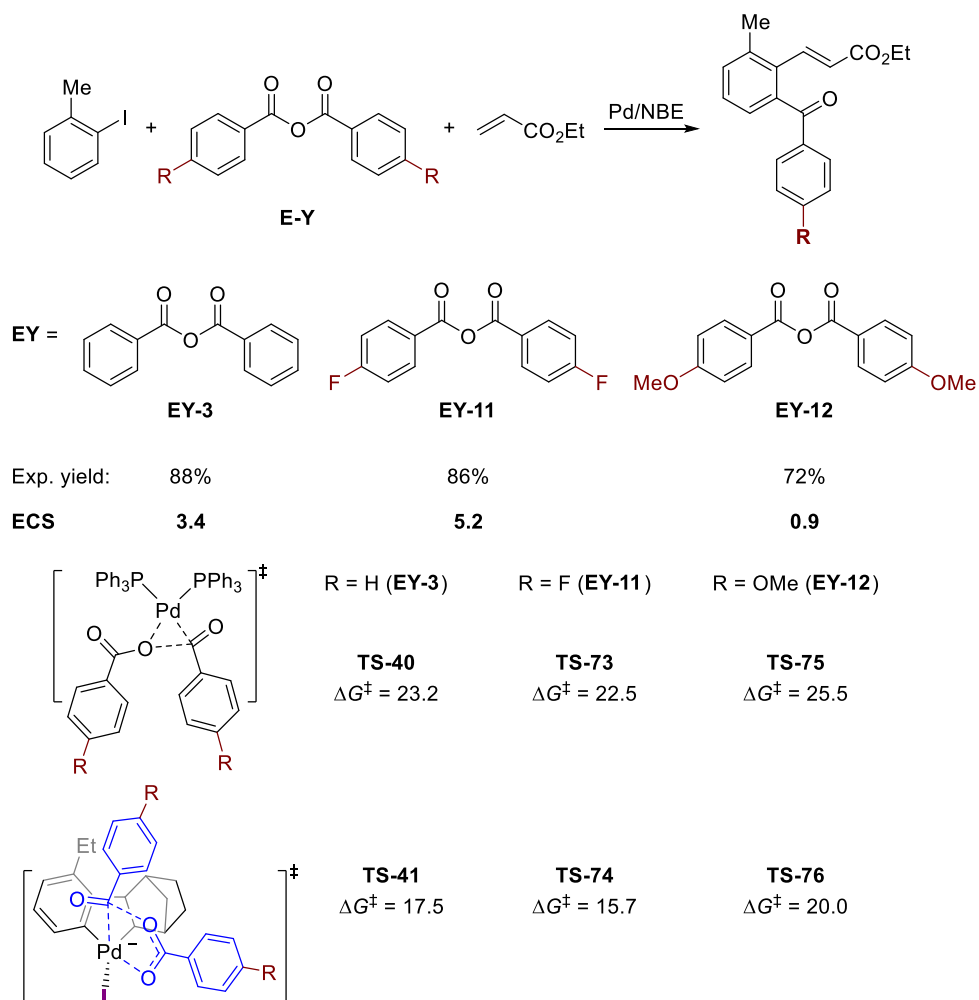


Fig. S27 Calculated electrophile compatibility score (ECS) of substituted anhydrides with **ArX-1** in Pd/NBE-catalyzed arene acylation reactions.

We next studied the electronic effects of anhydride electrophiles in acylation reactions. Two new anhydride electrophiles with an electron-withdrawing (-F) and an electron-donating (-OMe) group at the para position were calculated (Fig. S27). The calculated ECS with both acyl electrophiles are positive, indicating that they are both compatible with **ArX-1** in the Pd/NBE-catalyzed acylation reactions. The computational results also suggest that the electron-withdrawing group (-F) decreases the barrier of oxidative addition. The slightly lower yield in the reaction with **EY-12** is consistent with its relatively low ECS (0.9 kcal/mol), which is due to the higher barrier of oxidative addition with this electrophile.

In addition, we calculated the ECS between a bulky hydroxyl amine nucleophile (*i*Pr₂N-OBz) and **ArX-1** (Fig. S28). Our calculations indicated this electrophile is not compatible with **ArX-1**

(ECS = -9.2) due to the higher barrier (30.1 kcal/mol) in the oxidative addition of $i\text{Pr}_2\text{N-OBz}$ to ANP. This prediction is consistent with unpublished experimental results from the Dong group where no amination product was observed when this electrophile was used (Fig. S28). The bulky substituents ($i\text{Pr}$) on the N decreases the reactivity of $i\text{Pr}_2\text{N-OBz}$ with ANP. These results further demonstrate that the electrophile compatibility score (ECS) is reliable for the prediction of steric effects on electrophile compatibility.

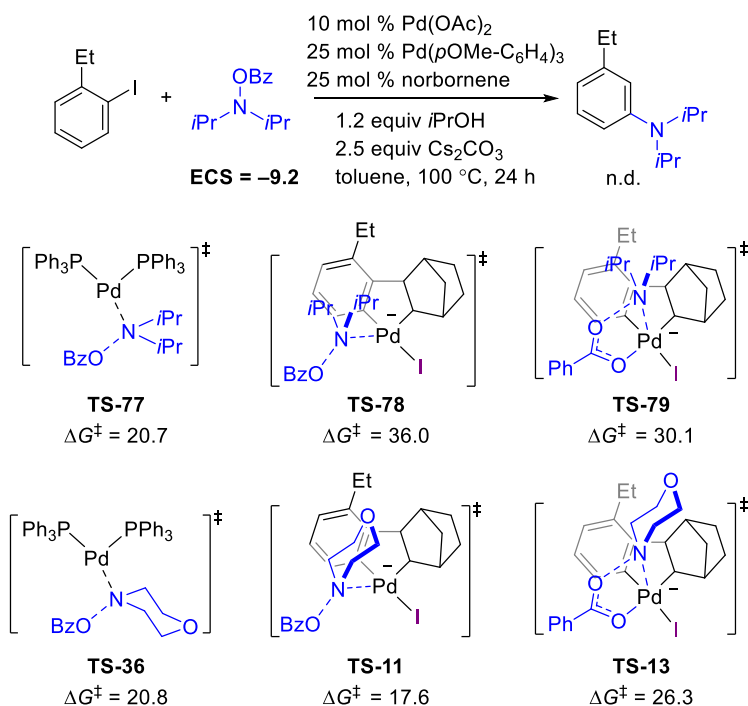


Fig. S28 Calculated electrophile compatibility score (ECS) of $i\text{Pr}_2\text{N-OBz}$ with **ArX-1** in Pd/NBE-catalyzed arene amination reaction.

15. Predicted compatibility scores (ECS) of electrophiles (EY-1~9) with different aryl halides (ArX-1~5)

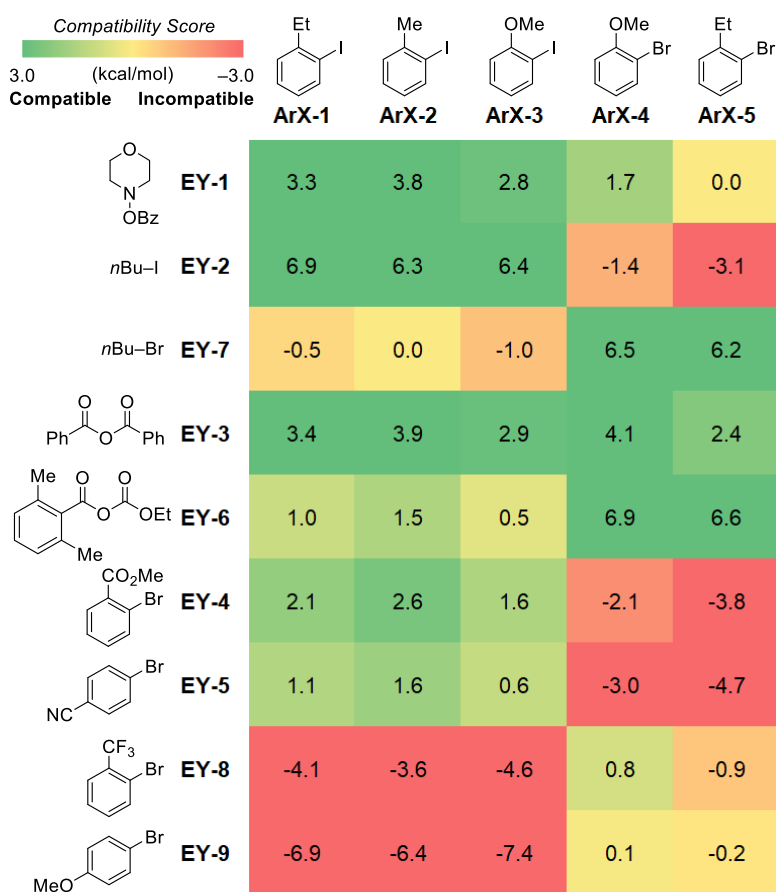


Fig. S29 Predicted compatibility scores (ECS) of electrophiles (EY-1~9) with different aryl halides (ArX-1~5).

16. Anion effects on the pathway selectivity of C–N reductive elimination

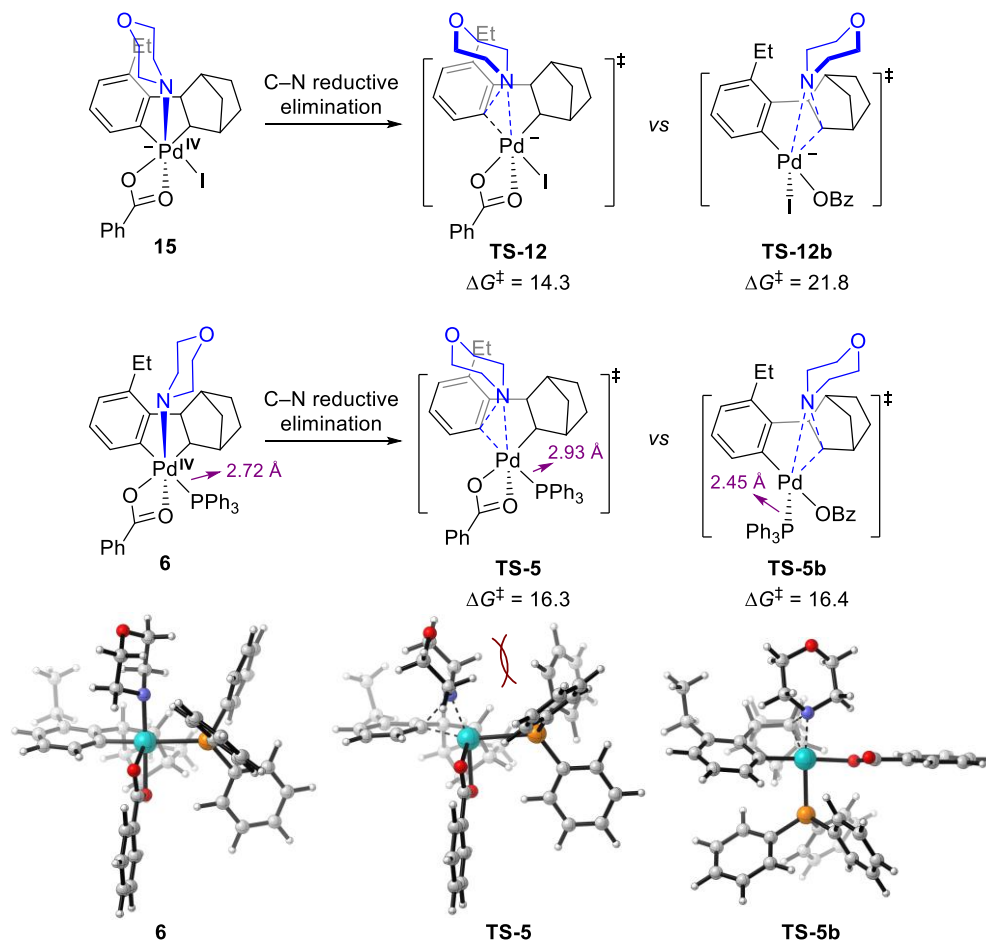
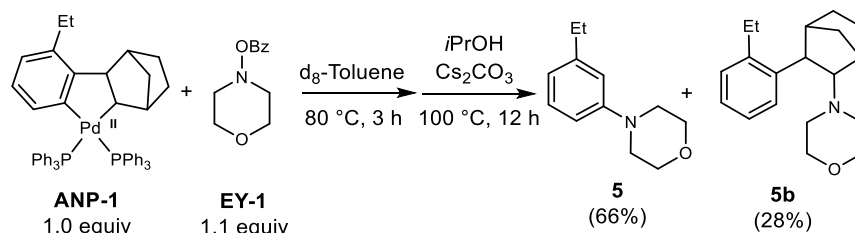


Fig. S30 The pathway selectivity of C(*sp*²)-N versus C(*sp*³)-N reductive elimination from iodide and PPh₃-supported Pd(IV) complexes.

Our computational results suggested that the C(*sp*²)-N reductive elimination from iodide-ligated Pd(IV) complex **15** is favored over the C(*sp*³)-N reductive elimination (Fig. S30). This result is consistent with the generally observed trend that favors reductive elimination with an *sp*² carbon center over an *sp*³ carbon due to more favorable electronic and steric effects in the C(*sp*²)-X (X = C and N) bond formation.² In the reductive elimination from the PPh₃-ligated Pd(IV) complex **6**, this selectivity is diminished. Transition states **TS-5** and **TS-5b** have comparable energies. This is because **TS-5** (the C(*sp*²)-N reductive elimination TS) is destabilized due to steric repulsions with the PPh₃ ligand. Because **TS-5** is a six-coordinate octahedral structure while **TS-5b** is a five-coordinate square-based planar structure, **TS-5** is sterically more encumbered. In

particular, there are substantial repulsions between the PPh₃ ligand and the morpholino group, which conformation is flipped in the TS and points the six-membered ring towards the PPh₃. In addition, the *syn*-periplanar conformation between the PPh₃ and the bridge-head carbon on the norbornyl group also increases the steric repulsions. These steric repulsions can be evidenced by the very long Pd–P bond distance in **TS-5** (2.93 Å). By contrast, steric repulsions with PPh₃ are much smaller in **TS-5b** because PPh₃ is *trans* to the morpholino group and *cis* to an empty coordination site. In comparison, when the PPh₃ is replaced with a smaller iodide ligand, steric repulsions in **TS-12** are much less significant, leading to higher selectivity in the iodide-bound reductive elimination pathways.

17. Experimental procedure



In a nitrogen-filled glovebox, an oven-dried 4 mL vial was charged with **ANP-1** (41.5 mg, 0.05 mmol, 1.0 equiv.) and **EY-1** (1.1 equiv.). Toluene-d₈ (2 mL) was added. The vial was tightly sealed, transferred out of glovebox, and stirred on a pie-block preheated to 80 °C for 3 hours. The vial was transferred back to the glovebox. Isopropanol (20.7 mg, 0.1 mmol, 2.0 equiv.) and Cs₂CO₃ (32.6 mg, 0.1 mmol, 1.0 equiv.) was added to the reaction mixture. The mixture was further heated to 100 °C for 12 hours. Upon completion of the reaction, the mixture was filtered through a thin pad of silica gel. The filter cake was washed with ethyl acetate, and the combined filtrate was concentrated. The yields of **5** and **5b** were analyzed using crude ¹H NMR spectrum with 1,3,5-trimethoxybenzene as the internal standard (Fig. S31).

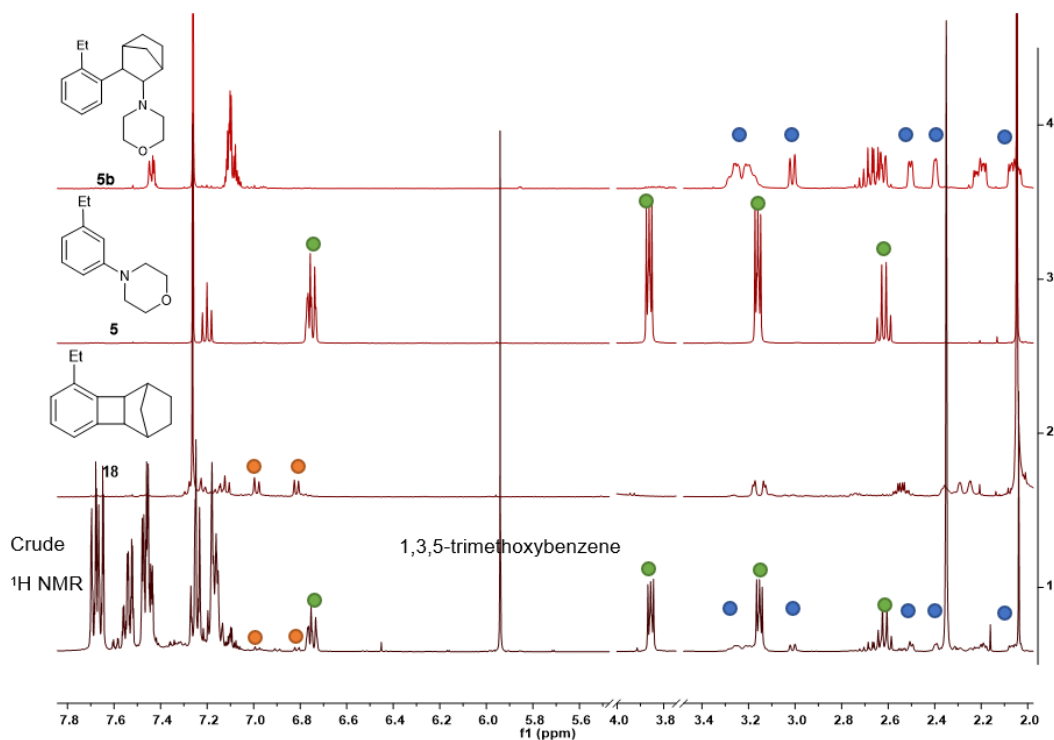


Fig. S31 Determination of yields of **5** and **5b** through crude ^1H NMR.

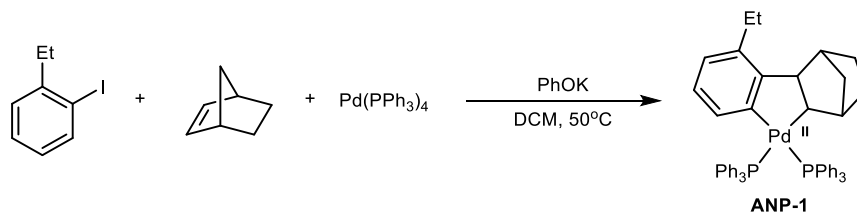
5: ^1H NMR (400 MHz, Chloroform-*d*) δ 7.20 (t, $J = 7.8$ Hz, 1H), 6.78 – 6.72 (m, 3H), 3.91 – 3.83 (m, 4H), 3.22 – 3.11 (m, 4H), 2.62 (q, $J = 7.6$ Hz, 2H), 1.26 (t, $J = 7.1$ Hz, 3H). Compound **5** is a known compound, the ^1H NMR spectrum matches literature report.¹

5b: ^1H NMR (400 MHz, Chloroform-*d*) δ 7.44 (dd, $J = 5.7, 2.7$ Hz, 1H), 7.14 – 7.05 (m, 3H), 3.33 – 3.11 (m, 4H), 3.01 (d, $J = 8.1$ Hz, 1H), 2.77 – 2.59 (m, 3H), 2.51 (d, $J = 4.6$ Hz, 1H), 2.44 – 2.36 (m, 1H), 2.25 – 2.16 (m, 2H), 2.10 – 2.00 (m, 2H), 1.94 (dt, $J = 10.0, 2.0$ Hz, 1H), 1.75 – 1.49 (m, 3H), 1.33 – 1.24 (m, 2H), 1.21 (t, $J = 7.6$ Hz, 3H).

Conditions for obtaining the crystal **VIII**

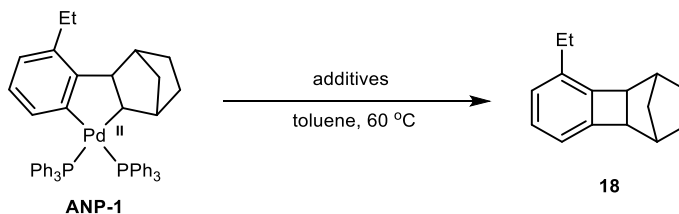
In a nitrogen-filled glovebox, an oven-dried NMR tube equipped with a J. Young valve was charged with **ANP-1** (83.0 mg, 0.1 mmol, 1.0 equiv.) and **EY-1** (1.1 equiv.). Toluene- d_8 (1 mL) was added. The NMR tube was tightly sealed, transferred out of the glovebox, and stirred on an oil bath preheated to 80 °C for 3 hours. NMR analysis of the crude reaction mixture showed complete conversion of **ANP-1**. After being transferred into the glovebox, the NMR tube was stored at room temperature for 10 days. During this period of time, a yellow crystal slowly

precipitated out, and it was subjected to the X-ray analysis (See attached cif file for details).



ANP-1 was synthesized according to a known procedure.³ In a nitrogen-filled glovebox, an oven-dried 8 mL vial containing a magnetic stir bar was charged with Pd(PPh₃)₄ (231 mg, 0.2 mmol), 1-ethyl-2-iodobenzene (232 mg, 1.0 mmol), norbornene (94 mg, 1.0 mmol), KOPh (53 mg, 0.4 mmol) and 5 mL of dry DCM. The vial was capped tightly, and the mixture was vigorously stirred in a 50 °C oil bath for 12 h. After cooled to room temperature, the solid was filtered away in the glove box and the filtrate was concentrated to dryness. The residue was dissolved in dry diethyl ether (7 mL) at room temperature in the glove box and the pure complex slowly precipitated out as white solid, upon standing at room temperature (126 mg, 76% yield). The white solid was filtered and dried under vacuum.

¹H NMR (400 MHz, Chloroform-*d*) δ 7.53 (t, J = 8.6 Hz, 6H), 7.38 (t, J = 8.4 Hz, 6H), 7.26 (q, J = 6.3, 5.4 Hz, 3H), 7.15 (dt, J = 13.7, 7.3 Hz, 9H), 7.05 (t, J = 7.0 Hz, 6H), 6.65 (t, J = 8.3 Hz, 2H), 6.29 (t, J = 6.8 Hz, 1H), 3.11 (s, 1H), 2.68 (m, 3H), 2.35 (d, J = 8.5 Hz, 1H), 2.25 (s, 1H), 2.17 (s, 1H), 1.23 (m, 4H), 1.01 (m, 3H), 0.01 (s, 1H).



In a nitrogen-filled glovebox, an oven-dried 4 mL vial was charged with **ANP-1** (41.5 mg, 0.05 mmol, 1.0 equiv.) and corresponding additives (1.1 equiv.). toluene (1 mL) was added. The vial was tightly sealed, transferred out of glovebox, and stirred on a pie-block preheated to 60 °C for 50 min. Upon completion of the reaction, the mixture was filtered through a thin pad of silica

gel. The filter cake was washed with ethyl acetate, and the combined filtrate was concentrated. The yield of **18** was analyzed using crude ^1H NMR spectrum with 1,3,5-trimethoxybenzene as the internal standard.

Compound **18** is a known compound, the ^1H NMR spectrum matches literature report.⁴

^1H NMR (400 MHz, Chloroform-*d*) δ 7.13 (t, $J = 7.5$ Hz, 1H), 6.99 (d, $J = 7.9$ Hz, 1H), 6.82 (d, $J = 7.2$ Hz, 1H), 3.20 – 3.11 (m, 2H), 2.55 (dq, $J = 7.7, 4.2$ Hz, 2H), 2.30 (dt, $J = 3.0, 1.5$ Hz, 1H), 2.26 (dt, $J = 3.1, 1.5$ Hz, 1H), 1.66 – 1.57 (m, 2H), 1.25 (t, $J = 7.7, 3\text{H}$), 1.22 – 1.17 (m, 2H), 0.99 – 0.94 (m, 1H), 0.91 – 0.85 (m, 1H).

18. X-ray crystallography data

Crystal data

$C_{44}H_{46}NO_3PPd \cdot C_7H_8$	$F(000) = 906$
$M_r = 868.32$	
Triclinic, P	$D_x = 1.395 \text{ Mg m}^{-3}$
$a = 10.4514 (5) \text{ \AA}$	Mo $K\alpha$ radiation, $\lambda = 0.71073 \text{ \AA}$
$b = 10.4712 (5) \text{ \AA}$	Cell parameters from 9926 reflections
$c = 19.8173 (10) \text{ \AA}$	$\theta = 2.4\text{--}27.4^\circ$
$\alpha = 80.720 (1)^\circ$	$\mu = 0.53 \text{ mm}^{-1}$
$\beta = 80.719 (1)^\circ$	$T = 100 \text{ K}$
$\gamma = 76.985 (1)^\circ$	Prism, clear colourless
$V = 2067.73 (17) \text{ \AA}^3$	$0.04 \times 0.04 \times 0.03 \text{ mm}$
$Z = 2$	

Data collection

Bruker SMART APEX2 area detector diffractometer	9515 independent reflections
Radiation source: microfocus sealed X-ray tube, Incoatec I μ s	7555 reflections with $I > 2\sigma(I)$
Mirror optics monochromator	$R_{\text{int}} = 0.050$
Detector resolution: $7.9 \text{ pixels mm}^{-1}$	$\theta_{\text{max}} = 27.5^\circ$, $\theta_{\text{min}} = 2.2^\circ$
ω and φ scans	$h = -13 \text{ } 13$
Absorption correction: multi-scan SADABS-2016/2 (Bruker,2016/2) was used for absorption correction. $wR2(\text{int})$ was 0.1101 before and 0.0545 after correction. The Ratio of minimum to maximum transmission is 0.9155. The $\lambda/2$ correction factor is Not present.	$k = -13 \text{ } 13$
$T_{\text{min}} = 0.683$, $T_{\text{max}} = 0.746$	$l = -25 \text{ } 25$
44714 measured reflections	

19. References

1. Dong, Z., Lu, G., Wang, J., Liu, P., and Dong, G. (2018). Modular ipso/ortho Difunctionalization of Aryl Bromides via Palladium/Norbornene Cooperative Catalysis. *J. Am. Chem. Soc.* *140*, 8551-8562.
2. (a) Ananikov, V. P., Musaev, D. G., and Morokuma, K. (2005). Theoretical Insight into the C–C Coupling Reactions of the Vinyl, Phenyl, Ethynyl, and Methyl Complexes of Palladium and Platinum. *Organometallics* *24*, 715-723. (b) Madison, B. L., Thyme, S. B., Keene, S., and Williams, B. S. (2007). Mechanistic study of competitive sp^3 - sp^3 and sp^2 - sp^3 carbon-carbon reductive elimination from a platinum (IV) center and the isolation of a C-C agostic complex. *J. Am. Chem. Soc.* *129*, 9538-9539.
3. Wu, X., and Zhou, J. S. (2013). An efficient method for the Heck-Catellani reaction of aryl halides. *Chem. Commun.* *49*, 11035-11037.
4. Catellani, M., and Cugini, F. (1999). A catalytic process based on sequential ortho-alkylation and vinylation of ortho-alkylaryl iodides via palladacycles. *Tetrahedron* *55*, 6595-6602.